



Institute of Earth Sciences
University of Iceland

école
normale
supérieure
paris-saclay

Mechanical engineering
department
École Normale Supérieure
Paris-Saclay

Predoctoral year of research abroad report

Innovative characterization of magmatic domains: parametric inversion of finite-element models at Eyjafjallajökull volcano, and adapted level-set shape optimization

Théo Perrot



Supervisor
Freysteinn Sigmundsson

Tutor
Karine Lavernhe

September 2023 - June 2024

This work is part of a 9 months internship, called "year of research abroad" (ARPE), under the tutorship of Karine Lavernhe, teacher and research scientist. It is part of the master's degree program in mechanics I have been following at the Ecole Normale Supérieure Paris-Saclay in France. The host laboratory is the Institute of Earth Sciences (Jarðvísindastofnun Háskólangs) of the University of Iceland (Háskóli Íslands) in Reykjavík. I was working under the supervision of researcher Freysteinn Sigmundsson within the ground deformation team.



Acknowledgments

First of all, I would like to thank Freysteinn Sigmundsson for his amazing supervision, for the scientific exchanges and for giving me the freedom to go in the direction I wanted in my project, to explore geoscience, a field I knew nothing about before coming to Iceland, and to discover this beautiful country, always with his good advice.

I would also like to thank the Ground Deformation team for welcoming me and helping me with my research, especially Chiara Lanzi, Yilin Yang and Halldór Geirsson. Many thanks to Michelle Parks and Vincent Drouin for hosting me at the Icelandic Meteorological Office (IMO) and teaching me InSAR, and to the ISVOLC project team for the scientific emulation. Thanks to the staff at the Institute for their support and to Sveinbjörn Steinþórsson for taking me out into the field and teaching me the basics of geodetic surveying.

Of course, this year would not have been the same without Greta, Anna, Daniel, Nico, Jonas, Steffi, Martin, Ramon and Clémence, my dear friends. Thank you for the hikes, the skiing, the nights, the lunches and the beers together, you made my year abroad a long dream.

Thanks to Oddur Pallson and his family (Páll, Gúðbjorg, Arní, Jenny and their kids, Auður) for their warm welcome and making me fall in love with North Iceland. Thanks also to Bógi Ingimundarson for sharing his passion for geological phenomena and teaching me about farming in Iceland during the lambing season.

Finally, thanks to Sakina for her support during this year away from home, for visiting Iceland with me and for her spell-checking skills, which were of great help in correcting this report.

Glossary

caldera Surface depression formed by the draining of subsurface magma reservoirs after an eruption. [7](#)

DEM A Digital Elevation Model (DEM) is a 3D representation of the Earth's surface, typically created from data collected by satellite or airborne sensors, and can even be formed with InSAR data ([C](#)). DEMs provide detailed information about the shape and features of the terrain, including elevations, slope angles, and aspect values . [15, 17, 19](#)

dike A dike is a type of geological formation that consists of a wall-like structure of rock that intrudes into surrounding rocks, often formed by the injection of magma after a magma reservoir reach its critical pressure and opens. It is the kind of structure that leads to eruption when the magma reaches the surface. [12, 19, 44](#)

glacial isostatic adjustment Process by which the Earth's crust rebounds and readjusts after a massive weigh has been removed due to the viscoelastic behavior of the upper part of the mantle. This cause the ground to slowly rise and expand ove tens to thousands of years depending on the viscosity. This happens in Iceland because of the rapid deglaciation that took place since the XIXth century. [9](#)

magma Melted minerals and gaz inclusions formed in Iceland by decompression of the Earth mantle due to the divergent movement of the North-American and the Eurasian plates. Due to a lower density, the magma has an ascending motion in the crust and causes eruptions when it reaches the surface, becoming lava after degassing. Most magma in Iceland is basaltic, i.e containing 30 to 40% of silica (SiO_2) (Freysteinn Sigmundsson [2006](#)). [5, 7](#)

sill A sill is a type of geological formation that consists of a tabular or sheet-like body of magma and its a privileged shape for most of magma reservoirs between pre-existing layers of rocks. When it cools instead of erupting, these lens shaped features can be observed after erosion of the surrounding host rock. [19](#)

unrest Set of patterns revealing magmatic activity in a volcanic system such as : ground motions, seisms, anormal volcanic gaz concentration at the surface or intensified geothermal activity. [5, 7](#)

Contents

Acknowledgments	3
Glossary	4
Introduction	6
1 Parametric optimization of finite-element models of an inflation at Eyjafjallajökull	8
1.1 Context and objectives	8
1.2 Data	10
1.2.1 GNSS	10
1.2.2 InSAR	11
1.3 Method	13
1.3.1 Mechanical problem	13
1.3.2 eyjaFEM software pipeline	15
1.3.3 Global optimization	18
1.4 Results	19
1.5 Limits and perspectives	22
2 Level-set shape optimization applied to magma domain inversion	23
2.1 Presentation	23
2.2 Article	23
Conclusion	40
Appendices	43
A Overview of Iceland geology	43
B Global Navigation Satellite System (GNSS)	45
C Interferometric Synthetic Aperture Radar (InSAR)	47
D Geodetic analytical models	48
E Pipeline benchmarking	49
F Additional figures	50
References	56

Introduction

With no less than 32 volcanic systems, Iceland is one of the most active place on Earth regarding volcanism, due to its peculiar geological settings (cf. A). The [magma](#) coming from the mantle is triggering eruption, but is often stored in intermediate reservoirs within the shallowest part of the crust. Hence, being able to describe the state of these magma reservoirs (or domains) is a central question in geophysics, for risk assessment as well as for scientific purposes, in order to better understand the subsurface volcanic processes and the mechanisms triggering eruptions. Quantities such as the location, the depth, the volume, the extent or the internal pressure of the domain can depict its current level of activity. Thus, obtaining an accurate estimation of these parameters is crucial for risk assessment.

However, there is no straightforward way to get this information, as the domain can only be tracked by indirect means. In this respect, ground displacement within the volcanic area is a good proxy : inflations, deflations and other more complex patterns of ground movements may indicate recharge, cooling and more, happening under the volcano (Paul Segall [2010](#), Freysteinn Sigmundsson, Parks, Pedersen, et al. [2018](#)). Therefore, geophysicists are facing an inverse problem, namely how to determine the causes of a phenomenon using its observable consequences. By essence, the amount of valid solutions (i.e valid sets of parameters) is infinite; thus, the goal of this work and of the geophysics community more generally is to find the *most likely*, the *best* solution in regard to the available information (Menke [2012](#)).

Eyjafjallajökull, famous for its eruption causing air traffic disruption in 2010, is one of the most active Icelandic volcanic systems and is the case study of this work. It is still in state of [unrest](#) and ground movements have been observed on its surface since 2010.

In the first chapter of this report [1](#), we study a post-eruptive inflation event taking place at Eyjafjallajökull between 2011 and 2015 that is yet to be studied in the literature. We present the gathering and processing of relevant geodetic displacement data. Then, we describe the use of a Python pipeline based on the finite element (FEM) code Castem (La Borderie [2017](#)), that we developed in the hope of solving for the main parameters of the magmatic source in cause. This was achieved thanks to a parametrized optimization loop modifying the numerical problem parameters at each iteration to best fit the geodetic data.

In the second chapter, we take a step back to experiment a new approach to the problem: instead of relying on a parametrized optimization implying strong assumptions

on the shape of the domain, we modified and adapted a shape optimization algorithm presented in Dapogny and Feppon 2023 to explore new shapes describing the source. Instead of minimizing the compliance of a domain as it is often the case in engineering, the algorithm is allowed to modify the shape and topology of the source to minimize the error function modelling the difference between an observed and a modelled displacement field. Finally, we apply this method on a real life case: an inflation event that happened in South East Iceland in 2022. This chapter is composed by a brief introduction and the preprint text of an article presenting the method and the first results, which will be submitted to a peer-reviewed journal in the next months.

A general conclusion of the work is given in chapter 2.2 as well as challenging perspectives for future work in the domain of volcano geodesy.

Several appendices explaining the basic concepts in use in geophysics (at the end of the document) as well as a glossary (above the table of contents) are given in this report, and may be of interest for a reader unfamiliar with geosciences.

Parametric optimization of finite-element models of an inflation at Eyjafjallajökull

1.1 Context and objectives

Eyjafjallajökull is a central intraplate volcano located in the South Iceland Volcanic Flank Zone, far from the main rifting area (see appendix A and fig.1.1). Hence, it is considered as a cold structure. It also differs from other Icelandic volcanic systems because it is not transected by any fissure swarms as explained in Freysteinn Sigmundsson, Einarsson, et al. 2020. A small 2.5 km wide [caldera](#) is on top, covered by a 50-200 meters thick glacier (Belart et al. 2019). For a better understanding of the settings, the reader can refer to the appendix A, which contains more details on geological and tectonic settings of Iceland. See the second page picture for a view of the North flank of the volcano.

The volcano erupted 4 times since the Icelandic settlement (872 CE). The first three eruptions were followed by an eruption at Katla, the neighbouring volcano (Guðmundsson and Höskuldsson 2019). The last eruption took place in 2010, after 18 years of [unrest](#). It started in March with a first small effusive phase on the flank (cover picture of the report), which was followed one month later by the explosive eruption at the summit causing air-traffic disruption in Europe, studied in detail by Freysteinn Sigmundsson, Hreinsdóttir, et al. 2010.

The magmatic system of the volcano active prior to and during 2010 is a complex network of sills fed from the mantle. Broadly two kinds of magma have been exhibited during the 2010 eruptions and might be found in the volcano : a basaltic [magma](#) coming directly from the mantle (with a low percentage of SiO_2 - around 48% for lava of the effusive phase) and a trachyandesite magma, richer in silicate (58% SiO_2 for the explosive phase) which is likely to be formed afterwards, drawing from long term storage in the shallowest part of the crust ([ibid.](#)).

The ground displacement has been continuously monitored during the events. The co and post-eruptive deformation signals showed a rapid deflation of the magma domain in cause due to the ejected material.

However, few is known on the evolution of the deformation afterwards and so on the evolution of the magma domain. The volcano has been monitored, and although no worrying signals have been detected, it has not been studied in details.

Therefore, a first question occurs : **What processes took place inside the volcano after the 2010 eruption ?**

To tackle this question, we choose to focus on the 2011-2015 inflation, revealed by the

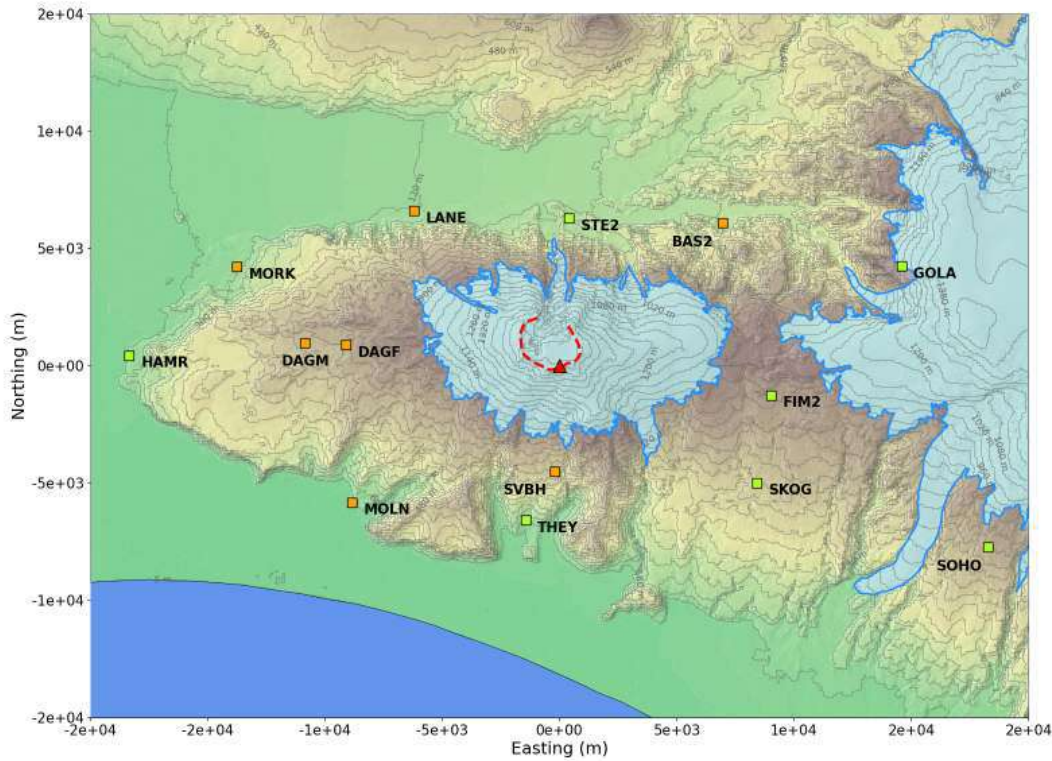


Figure 1.1: East-west elongated structure of Eyjafjallajökull. The summit (1651m high, 63.61980°N, -19.61505°W) marked with the red triangle is chosen as local origin for this study. The coordinate system is shifted cartesian ISN2016 at the summit (Valssson 2019). Glaciers are outlined in blue, with the Eyjafjallajökull summit glacier in the center and Myrdalsjökull east of it. The summit caldera is outlined with the red dashed line. Locations of GNSS stations included in the dataset are marked with a square, orange for the campaign sites and green for the continuous ones.

processing of displacement data on the volcano (described below in 1.2) as phenomenon of main interest. We assume that the observed movement is triggered by a pressure increase in a magma chamber located in the subsurface of the volcano, in accordance to what has been concluded on the inflation preceding the 2010 eruption **sigmundsson2010**. This hypothesis leads to a narrower research question :

What are the characteristics of the magma reservoir causing the 2011-2015 inflation and is such a feature realistic ?

As detailed before, this question raises an inverse problem that we aim to solve with optimization based on numerical simulations. This procedure is described afterwards, in the section Method (1.3). Finally, the inferred characteristics (namely the geometry and position) of the reservoir will be presented in the section Results (1.4), as well as a discussion on the limits of the presented approach.

1.2 Data

1.2.1 GNSS

Eyjafjallajökull and its neighbour Katla are monitored by a dense network of Global Navigation Satellite Systems (GNSS, see appendix B for more details on the method) stations. After a field campaign in September 2023 to retrieve new positions of campaigns site, we formed a dataset of displacement time series at 12 sites (both continuous and campaign) around the volcano, selected for their good coverage of the entire period 2010–2023. The raw time series were obtained using the GAMIT/GLOBK (Floyd 2024) software on the raw observation files.

We then applied different corrections in order to observe only the signal of interest, namely the local ground motions due to local phenomena, such as volcanic activity. First, we removed the plate motion from the horizontal components (East and North) with the ITRF2014 (Altamimi et al. 2016) model, assuming that all stations are located in the stable interior of the Eurasian plate as shown on Fig. A5 (see appendix A for details about the plate motion). We also removed from the Up component the uplift due to regional glacial isostatic adjustment, estimated to reach around $7\text{--}8 \text{ mm yr}^{-1}$ in this area according to observations and models from Drouin and Freysteinn Sigmundsson 2019.

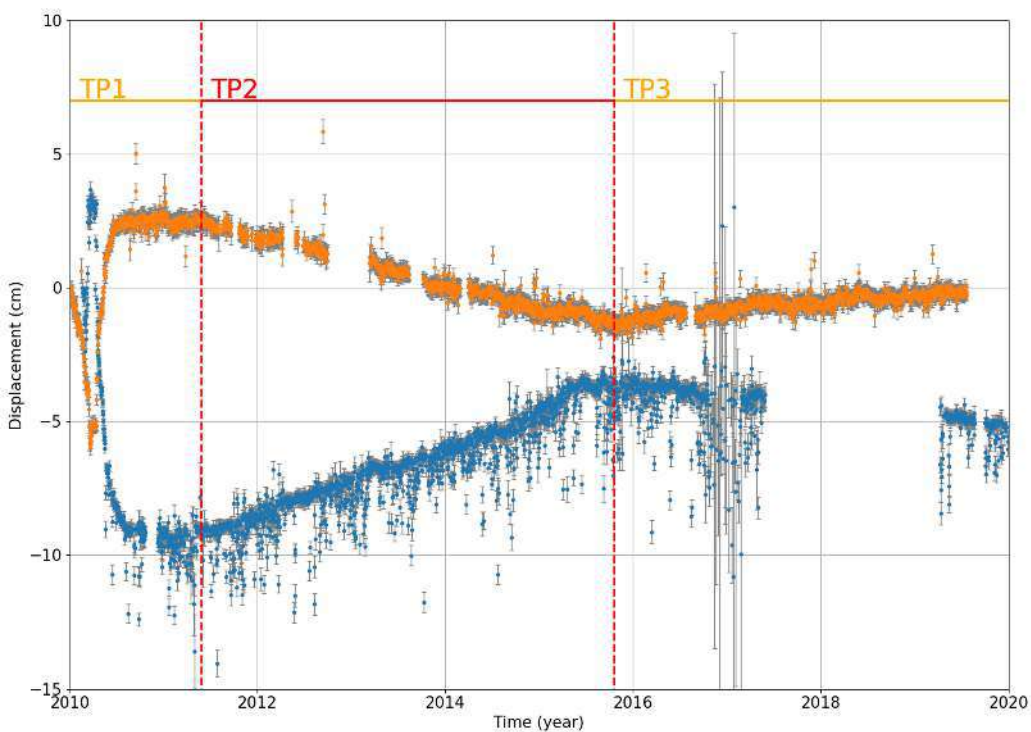


Figure 1.2: Displacement time-series at *THEY* and *STE2* (respectively located South and North of the caldera, see fig. 1.1). *TP1* refers to the eruptive inflation and deflation of the magma source of the 2010 summit eruption Freysteinn Sigmundsson, Hreinsdóttir, et al. 2010, *TP2* is the constant inflation of interest in this paper and *TP3* indicates a constant deflation with the stations converging towards the summit at a lower rate.

Looking at the de-trended time series from the two continuous sites *THEY* and *STE2*, which are closest to the summit caldera, 3 main trends can be identified (see Fig. 1.2). The post-eruptive inflation period TP2, where the two stations are diverging from each other, is the one we are interested in. From $2011.45 \pm 0.2\text{yr}$ to $2015.82 \pm 0.2\text{yr}$ (limits estimated by visual inspection of the time series), both stations show a remarkably constant displacement rate.

As mentioned before, we chose to focus on the modelling of the time period *TP2* as a case study. Hence, further data processing has been performed regarding the 2011-2015 inflation period.

The time series we obtained shows a linear increase in displacement. Due to its linearity, this inflation can be entirely characterized by the total displacement for the full-time period at the surface of the volcano following. As presented in section 1.3, the elasticity theory works well for this type of event because there is no time consideration.

Thus, the total displacements have been estimated by calculating the displacement rates with a least-squares fit at each site and for each component (East, North, Up). The obtained speeds are easily integrated to total displacement, knowing the duration of the event. We ended up with a map of the total displacements at each site. This map showed a north-westward trend, which we attributed to ground motion from the Katla volcano. Since our models were focused on Eyjafjallajökull, we decided to remove this trend from the total displacement vectors by removing the mean of the horizontal displacements at *SKOG*, *SOHO*, *FIM2* and *GOLA* from all stations, as these four stations are closest to the Katla volcano and therefore more likely to be affected by its movements. Finally, we obtain the total displacements at each site for the inflation period 2011-2015, shown in figure 1.3. The general trend observed is a divergent pattern, representative of a slow inflation (the fastest stations *STE2* have an average velocity of ??mm/yr).

Out of curiosity we also processed the data for the following *TP3* period and a deflation pattern is clearly visible on the figure A6. However, it is out of the scope of our study.

1.2.2 InSAR

Interferometric satellite radar (InSAR) observations were used to obtain global displacement maps of the area, giving information where no GNSS station are available. This is possible at the price of a poor temporal coverage, the time step depending on the period between two successive passes of the satellite. The coverage of the area is however incomplete due to the summit glacier and the proximity of the ocean, which both cause decoherence of the signal (Fletcher 2007). See appendix C for explanation on the method and of the associated vocabulary.

We first used the A32 ascent track of the Cosmo SkyMed satellite and generated interferograms from 2011 to 2015 using the DORIS software developed by Kampes and Usai 1999. We excluded the interferograms with poor quality (decoherence due to snow cover or strong atmospheric signal, see fig. A7 to see all the interferograms used in the process). As for the GNSS data, we are interested in the total displacement of the inflation period. Therefore, we carried out a time series processing on the formed interferograms by performing a permanent scatter analysis on StAMPS, algorithm developped in A. Hooper, P. Segall, and Zebker 2007 and improved in Andrew Hooper et al. 2012. At the end of the process we obtained an unwrapped map of the line-of-sight (LOS) displacement rate, as shown on the figure A8. Finally, the LOS displacement map was produced by multiplying the rate value by the time length estimated from the GNSS time series.

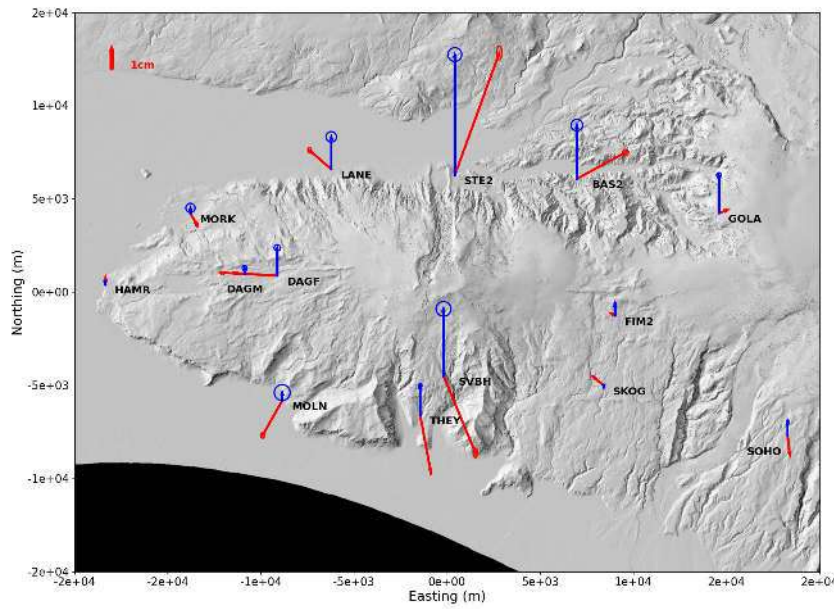


Figure 1.3: Total displacements between 2011 and 2015 at each GNSS site. The vertical and horizontal displacements are indicated by respectively blue and red arrows. The ellipses on the end of the arrows are the 99% confidence intervals.

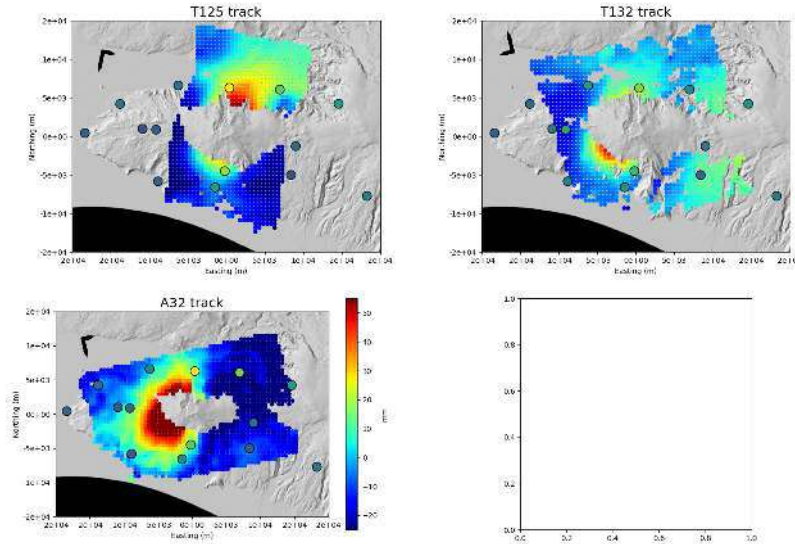


Figure 1.4: Downsampled map of the total displacement for the 2011-2015 inflation obtained after time-series analysis of the three InSAR tracks of the dataset: CSK A32, T125 and T132 (the two last being processed by M. Parks at the IMO) . Note that this is line-of-sight (LOS) projected displacement. The black circled dots are the GNSS displacements converted to LOS geometry for comparison, consistent with the InSAR observations.

Two patterns of deformation can be observed in this map. First, a local positive LOS signal near the summit indicates localized inflation in this area and is consistent with GNSS observations. However, another deformation pattern appears : it follows a line through the summit caldera, suggesting that the western and eastern sides of the volcano are moving away from each other. This is not observed in the GNSS time series. It is worth noting that this deformation signal could indicate processes taking place in the volcano at the end of the inflation period. A small [dike](#) intrusion, indicated by the linear pattern, cannot be excluded. However, such processes are outside the scope of this work, as the present study focuses only on the linear inflation of 2011-2015. We have therefore decided to remove this additional signal. It appears on interferograms dating from 2015 onwards, therefore we computed the displacement rate map using good quality interferograms from 2012 to 2014 only. Since the deformation observed at the summit is assumed to be at a constant rate over the entire inflation period from GNSS observations, this should not affect the estimated velocity. Finally, we obtained a total LOS displacement map consistent with the GNSS observations and showing only the summit inflation (see Fig. 1.4).

Two additional processed tracks from the TerraSarX satellite were provided by M. Parks, geophysicist at the Icelandic Meteorological Office (IMO), and shown on fig 1.4. These tracks being respectively ascending and descending, more information can be retrieved because it offers two different LOS geometry (see C). Hence, we formed a richer InSAR dataset with 3 InSAR tracks : CSK A32, TSX T125 and TSX 132.

We tried to get a 3D displacement map of the inflation to merge the InSAR and GNSS datasets in one, but the results were not convincing enough to be used as input data, as shown figure A9.

1.3 Method

From the observed displacement field, we search for the parameters describing the magmatic source causing it. This implies two main conceptual steps. First, we need to define a well-posed mechanical problem including the parameters of the magma chamber in its formulation (sec. 1.3.1). Then we need a method to solve it for various values of the magma chamber parameters - this is the purpose of the software pipeline presented in section 1.3.2. Finally, the global optimizer (sec. 1.3.3) aims to find the best parameters for the magma chamber by minimizing the difference between the observed displacement field coming from the data gathered above, and the displacement field predicted by the model.

1.3.1 Mechanical problem

The problem is summarized by the diagram in figure 1.5.

The magma chamber is modelled as an empty cavity subjected to a uniform pressure field ΔP which accounts for the pressure change between the interior of the cavity and the surrounding lithostatic pressure (i.e. pressure existing within the crust because of its weight and additional loadings). This is a modelling simplification which is almost always done when modelling magmatic source because, in a first order, the fluid movements that happen in the magmatic chamber have little influence on the surface ground displacement. The important phenomenon to capture is that a reservoir is being pressurised by

new magma upwelling from the mantle, as explained by Freysteinn Sigmundsson, Parks, Pedersen, et al. 2018.

The medium in which the cavity is embedded is the earth crust. It is assumed to be homogeneous and isotropic in first order. It is also assumed to behave purely elastically.

Indeed, the displacement change at the surface is linear in time. Therefore, we suppose that it is the same for the pressure increase. We decided then to model the total pressure increase in the magma chamber. Therefore, this inflation can be studied in the scope of stationary model : the time is no longer an influencing parameter. The earth is thus considered as behaving in a purely elastic way, and any time-dependent effect is neglected. This assumption can be found commonly in the literature dealing with modelling, for example, the total inflation of a magma domain within a time period [REF].

The geometry free interface between the crust and the air is determined by the topography, and is not assumed to be flat. Indeed, topography is of influence because it affects the observed surface displacement by extending the amount of crust being displaced Dzurisin 2007. The sphericity of Earth is also neglected : the typical length of the problem l_0 is of the order of 10 km, far below Earth radius ($R_e = 6371\text{km}$): $l_0 \ll R_e$.

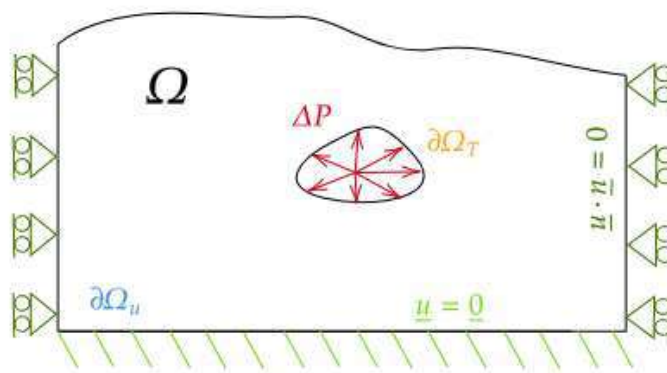


Figure 1.5: Diagram of the simplified mechanical problem. The domain is Ω , assumed to be homogeneous, isotropic and purely elastic, described only by the parameters E (Young's modulus) and ν (Poisson's ratio). The loaded boundary $\partial\Omega_T$ is subjected to the magmatic pressure ΔP : $\underline{\sigma} = \Delta P \underline{n}$ (where $\underline{\sigma}$ is the stress tensor and \underline{n} the unit vector normal to the boundary). The kinematically constrained boundary $\partial\Omega_u$ has as boundary condition no displacement ($\underline{u} = \underline{0}$) at the bottom and roller condition on the sides ($\underline{u} \cdot \underline{n} = \underline{0}$). Of course, $\partial\Omega_T \cap \partial\Omega_u = \emptyset$.

Once again, the problem is inverse: by partially knowing the displacement field, we want to find the loading characteristics, namely the geometry of the loaded boundary (the magma chamber) and the value of the loading (the pressure increase).

The most appropriate class of models in this respect are the analytical models described in the Appendix D. They are parametrized and the surface displacement is obtained instantaneously with the expression derived from the model. Thus, Bayesian inversion yielding strong results in the form of probability distribution (app. D).

However, they are limited by their simplicity and the strong hypotheses they require. For example, it would be impossible to take into account the complex topography of Eyjafjallajökull. Only simplified topographies such as conic edifice can be partially modelled by such models (ibid.).

On the other hand, numerical models allow a more detailed modelling. They are

often based on the finite element method (FEM), the most widely used numerical method for solid mechanics simulations. Complex geometries for magma sources and surface topography can be included. It is also possible to include advanced mechanical behaviours such as viscoelasticity, plasticity or poroelasticity, as well as other kinds of loadings such as the glacier loading, or tectonic stress (out of the scope of the present work). The possibilities are endless, limited only by computational time, which is the bottleneck of such models.

1.3.2 eyjaFEM software pipeline

In this regard, we built a software pipeline in Python connecting many software components in order to be able to design and run any finite element mechanical model. Finite element method (FEM) is classically in use to solve numerically solid mechanics problems. It is relevant here for its versatility: most of the geometries can be discretized and most of the behaviors can be solved (of course, some limitations exist but are beyond the complexity of the problem we implemented here).

Architecture

Several FEM software solutions exist for such an application, such as *Catia*, *COMSOL Multiphysics* or ABAQUS software suite, which enable the construction of models for geophysics (Greiner 2021, Schmidt et al. 2010) and even the execution of parametric inversion (Hickey and Gottsmann 2014, O’Hara 2023). However, as such software are not open-source or free, their use comes at a cost. Moreover, the lack of transparency on certain aspects of the resolution is not adapted to scientific investigation. Therefore, we decided to build a software pipeline called eyjaFEM, coded in Python around Cast3m scripts and relying on other components to extend the functionalities. The main aspects of this pipeline are shown in Fig. 1.6.

The overall performance of the pipeline was tested by benchmarking against an analytical model. After setting up an FEM model including a prestressed finite spherical cavity, we ran the entire pipeline to test each of its components. We compared the numerical surface displacement field with the analytical solution derived by Mac Tigue McTigue 1987. The residuals were less than 0.1 mm in each direction and no significant boundary effect was found, confirming the validity of the models. See appendix D for the detailed description of the benchmarking process.

To perform the inversion of the FEM models solved by Cast3m, a versatile software pipeline was implemented in Python. The idea was to build the components for each step of modelling (see 1.6). This enables the easy modulation of each step, and can then be inserted into an inversion loop, for example.

The pipeline starts with a **Geographer** module that generates Digital Elevation Models (**DEM**) in the appropriate formats, in the good coordinate system and at the desired resolution. The **Geometrician** module creates the specified geometry for the domain. It can include a source of any regular shape and topography taken from the **Geographer**. This module can then create a mesh for this geometry with variable element sizes. The user can specify patterns to refine certain areas of the mesh. This module is based on the powerful open-source mesher GMSH Geuzaine, Remacle, and Dular 2009. The **Mechanics** module then collects all the useful files and executes the required Cast3m script depending on the selected FEM simulation mode. At the moment, only one Cast3m script has been implemented for the basic elastic resolution, and another one including topological

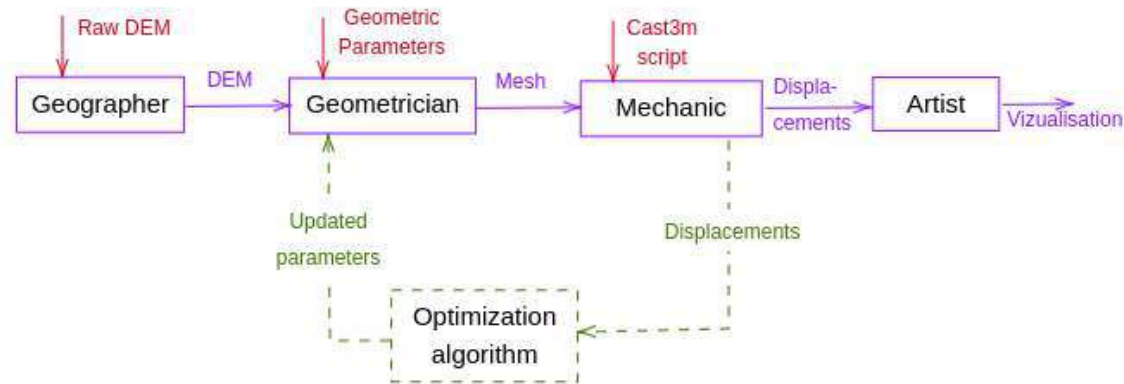


Figure 1.6: Architecture of the pipeline. The geodetic observations are processed by an object Topographer. It is then transmitted to an object Geometrician interfacing the open source meshing software GMSH Geuzaine, Remacle, and Dular 2009. The constructed mesh is then transferred to the Mechanic in charge of executing the CASTEM scripts. The results are then processed and visualized by the Artist. The optimization loop is ensured by Optimizer which calls the chosen optimization scheme.

optimization is under construction. Once the simulation is complete, all relevant output files are saved. Finally, the output can be visualized in different plots with the **Artist** module or in the visualization tool Paraview.

More details are given on the key components and how they work in the following paragraphs.

Geometry and meshing

Geometry definition and meshing are two operations that are handled by the **Geometrician** module, which communicates with the powerful software GMSH through its Python API. It was chosen over Cast3m's built-in basic mesher because it provides complex geometries and mesh definition that cannot be obtained using Cast3m.

The geometry core OpenCASCADE of GMSH Geuzaine n.d. enables us to define complex geometries, as showed in figure A10. The domain is a block, but the top surfaces follow the topography of the volcano given by the **DEM** of Landmaelingar Islands. OpenCASCADE handles surfaces generated by cloud points. Ellipsoidal surface is also generated for the source. From there, with operations such as intersection, differences and union, the full geometry is built.

The main quality of GMSH relies on the versatility of its meshing core. We want to minimize the computational time of the FEM models, because the aim is to use them in inversion loops, i.e. to simulate them thousands of times with different parameters. Hence, we tested several kinds of meshes with different element size distributions as shown in the figure 1.7 and used the same procedure as for the benchmarking to evaluate their quality.

After a trial-and-error process, we found that the most important regions to refine in order to ensure the accuracy of the surface displacements are the source (two coarse element sizes change the geometry of the source), the upper surface where the displace-

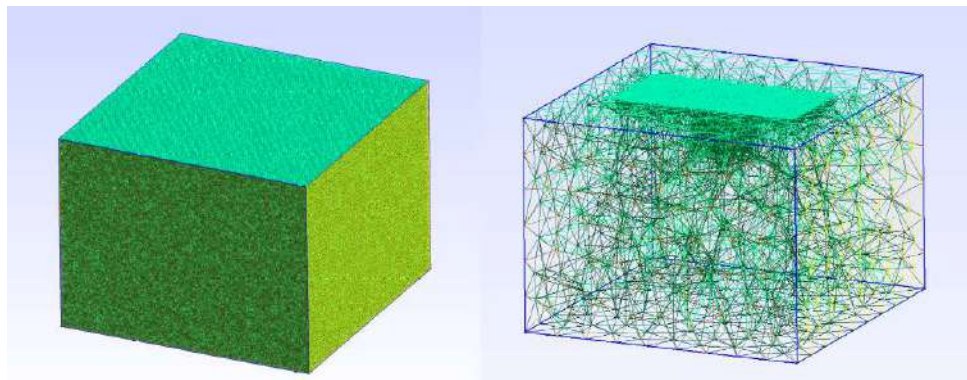


Figure 1.7: On the left, uniform mesh with an element size of 500m. On the right, the best mesh in terms of computational time and accuracy. We can see the refinement at the surface (the area of interest for comparing displacements) and around the source.

ments are calculated, and the zone closest to the source (subject to the highest strain values that can be underestimated if the mesh is too coarse). It is also important to keep a large coarse area around the zone of interest to mitigate boundary effects. Previous tests have shown that a good mesh quality of the source is crucial to obtain an accurate solution : therefore, the area in which the source is embedded is finely meshed, with an element size of 100 m at the source and 1km around the feasible boundaries (potential source locations). To minimize interpolation errors when calculating the surface displacement at the data location for comparison, the surface is fine-meshed with a resolution of 1km within the extent of the data locations (GNSS and InSAR points). This entire fine-meshed area represents a parallelepiped of dimensions $60 \times 60 \times 20 centred below the local origin (summit position). Its outer part is coarsely meshed (10 km elements) because no data of interest are computed here. Indeed, the only use of this part of the domain is to minimize boundary effects. Tetrahedrons were chosen as the element type because they have been proved to be efficient in accommodating all kinds of geometries, thus being suitable to handle the topography and element size gradients, and they are the computationally cheapest 3D elements with only 4 nodes. The full mesh is visible in figure??.$

The best mesh is the one shown on the left in the figure 1.7 because it has a reasonable meshing time (only 4.54s for meshing and solving on a personal class laptop, RAM of 16GB and processor AMD RYZEN 7 4800H) and shows a good agreement with the analytical solution with RMS values comparable to the uniform mesh: $\Delta U_x = 2.6e - 4m$ $\Delta U = 4.8e - 4m$.

Finite element solver

In order to remain flexible in terms of possible applications, we use the finite element solver Cast3m (or CASTEM) La Borderie 2017. This open-source code, developed by the French Alternative Energies and Atomic Energy Commission (CEA), includes a large number of mechanical behaviours (viscoelasticity, fracture, fluid-solid interfaces, hyperelasticity, orthotropy) that can be of interest to geophysicists. However, its functionality is limited to solving the FEM elements and the data manipulation or optimization functions are quite restricted. Thus, we designed the architecture ensuring that only this task is achieved by Cast3m, and all other data manipulation tasks are performed by the Python pipeline. To interact with Cast3m, we pre-wrote GIBIANE scripts (a scripting language developed to

interact with CASTEM) that are then filled and automatically executed by the module **Mechanician** of eyjaFEM.

In practice, for the inversions we ran, the forward model included :

- Isotropic linear elasticity. The elastic parameters taken at the surface are $E_0 = 30\text{GPa}$ and $\nu_0 = 0.25$.
- Topography from the nation-wide 2m **DEM** of Landmaelingar Islands, including the glacier which is here considered as bedrock.
- Spherical source with radius fixed at 800 m.

We do not include lithostatic pressure, tectonic stress or glacier loading, but such subtleties can be implemented using the power of finite element method. The total size of the domain reaches 60 km in the East, 50 km in the North and 30 km depth below sea level, with the topography extending to 1650 m above sea level.

This makes the solving time of the elastic problem of 1.5-2 s, which is reasonable if we aim to run 10000 problems in a row during an inversion procedure. See figure ?? where the solution given by Cast3m after running one forward model is shown.

1.3.3 Global optimization

Once the forward model part of the software is built, we are interested in solving the inverse problem. In the model we described above, the parameters that characterize the magmatic chamber are the pressure change ΔP , the radius of the source R , its location x, y and its depth z . As explained in Greiner 2021, R and ΔP can be switched with no influence on the surface displacement field, as long as the product $\Delta P R^3$ remains constant. Hence, in an inversion approach, we chose to fix R to avoid over-determination of the model. Hence, we can reformulate the inversion problem into an optimization problem: we aim to find the best value for vector of parameter $p = (\Delta P, x, y, z)$, i.e the value which minimizes the discrepancy between the observed (\vec{O}) and the modelled ($\vec{M}(p)$) displacement given by the value of an objective function J .

Here we defined J as :

$$J(p) = \gamma_1 J_G(p) + \gamma_2 J_{I1}(p) + \gamma_3 J_{I2}(p) + \gamma_4 J_{I4}(p) \quad (1.1)$$

with γ being the weights and J_G the GNSS error function and J_I the InSAR error function, which are basically RMS errors :

$$J_G^2(p) = \frac{1}{N^2} \sum_i^N (\vec{M}_i(p) - \vec{O}_i)^2 \quad (1.2)$$

Here, N is the number of observations and $M_i(p)$ the modelled displacement for the set of parameters p at the localization of the observation O_i . It is important to note that arbitrary weights γ_i are given to each dataset. These weight are set up before inversion to account for the confidence in the different datasets we have. Also, the relative order of magnitude the dataset may have (for example, there is many more points in InSAR observation) is taken into account by normalizing each J_i by its null-test $J_{i0}^2 = \frac{1}{N^2} \sum_i^N (\vec{O}_i)^2$ which corresponds to an error function with a null model, giving an idea of the weight of the dataset in itself.

With this set up, to tackle the inversion problem, a global optimization algorithm is employed to explore the vast parameter space $p \in \mathbb{R}^4$ and identify the optimal solution. In the global optimization paradigm, we try to explore the parameter space as efficiently as possible without assuming anything on the objective function to pinpoint the most plausible solution for the magmatic chamber properties Rios and Sahinidis 2013, and ensuring it not a local minimum (like local optimization), i.e

$$\min_{p \in \mathbb{R}^4} J(p) \quad (1.3)$$

Indeed, for us, each evaluation of J with a new p involves remeshing (because of the change in magma chamber position) and solving an elastic FEM model to compute the corresponding displacement field, which takes between 2 and 4 seconds.

In practice, we limit the search space to feasible bounds to pre-constrain the problem so that a minimum of assumptions is required. Typically, we search the pressure between 1 and 100 MPa, and the location within the boundaries of the meshed domain.

Global optimization is an entire active research field, and dozens of algorithms exist, as reviewed by Cartis, Roberts, and Sheridan-Methven 2022. We have limited our tests to two algorithms that have been shown to work on various tasks: DIRECT (Dividing Rectangle), first introduced by D. R. Jones, Perttunen, and Stuckman 1993, and BOBYQA (Bound Optimization by Quadratic Approximation), introduced by Powell 2009. In short, DIRECT works by estimating J in rectangular slices of the domain, which are themselves subdivided into slices where J is re-estimated when a new minimum is found. In BOBYQA, J is iteratively estimated with a local quadratic approximation valid in a trust region. In the trust region, a step is taken stochastically, and if the decrease of J is good enough, it is taken as the new iteration.

They have been revised and extended since (Donald R. Jones and Martins 2021) and remain relevant in our context. The first is purely deterministic and the second is stochastic, but both are derivative-free (they don't require an assumption about J' and don't try to approximate it at each iteration). We also tried other global optimization algorithms such as simulated annealing (Xiang and Gong 2000) and Bayesian Optimization (Shahriari et al. 2016) without satisfaction. Indeed, such an algorithm needs to be tuned with a consequent number of parameters, which makes its relevance less clear compared to DIRECT and BOBYQA, which do not need any tuning parameters if no termination criterion is specified.

In our test, the typical iteration budget we allowed was between 2000 and 5000 iterations, and we then took the best result p found among these tests, so we did not specify any termination criterion.

1.4 Results

We run optimization loops many times to evaluate its operation.

The influence of the radius was tested by setting different values for the sphere radius between 100 m and 1 km and it showed, as expected by theory (Greiner 2021), that the pressure change ΔP_{min} found after optimization was such that the product $Rs\Delta P$ remained constant.

Overall, BOBYQA showed better efficiency in converging to a minimum, even when the minima found by both algorithms were relatively close. However, the weighting of the data sets γ_i was the main influence.

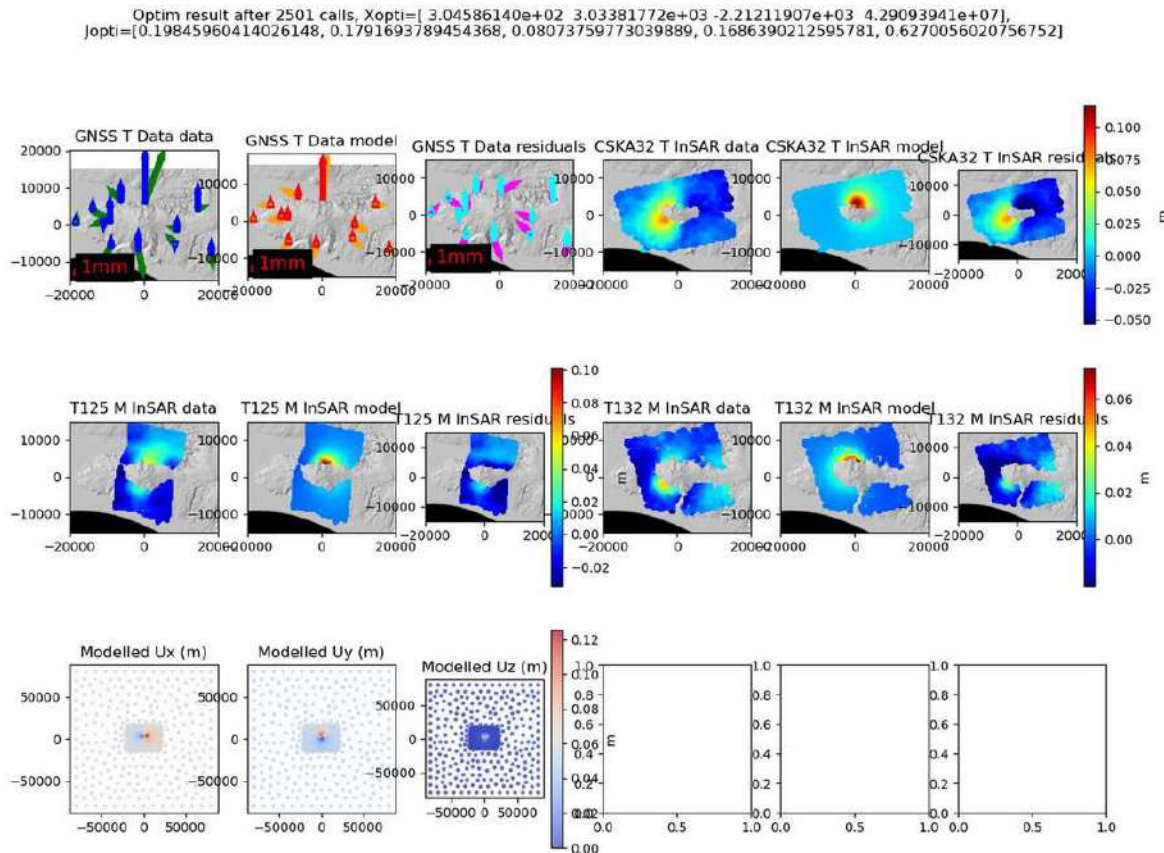


Figure 1.8: Best result found after 2500 evaluations of J . The relative weights of the datasets are $GNSS, CSKA32, T125, T132 = 7, 1, 1, 1$, which means that the GNSS account for 70% of the total weight and the InSAR tracks together for 30%. Each series of 3 maps corresponds to the data, the best model and the residual of each dataset. The last 3 maps correspond to the East, North and Up components of the best model. Note that the data points are not evenly distributed. As explained in section 1.3.2, the mesh is denser in the area near the summit to better interpolate the displacement at the data points. Therefore, there are more points where the displacement is calculated in this area. The best parameter vector found is $p_{\text{opt}} = (0.304\text{km}, 3.03\text{km}, -2.21\text{km}, 42.9\text{MPa})$ for a $J = 0.19$ (knowing that $J = 1$ is the value of J with only null tests).

On the figure 1.8 we show the best result obtained with DIRECT. Additional results obtained with DIRECT are shown in figures A12 and A13 but they are less relevant.

We compare the results in the table 1.1 with the results from Sigurðardóttir 2024 and from Freysteinn Sigmundsson, Hreinsdóttir, et al. 2010. Sigurðardóttir 2024 Modelled the same inflation event with the GNSS data we provided to her, using GBIS for inverting the source parameters based on a Mogi 1958 model. Freysteinn Sigmundsson, Hreinsdóttir, et al. 2010 reported the parameters of the deflation source responsible for the 2010 April summit eruption, also modelled Bayesian inversion but with a penny-shaped crack model (Fialko, Khazan, and Simons 2001).

The comparison leads us to conclude that the source that inflated is the same as the one that emptied in April 2010. Based on the volume estimates, about three times less magma recharged the reservoir after 2011 than what was erupted in 2010. This is consistent with the fact that no eruption was reported after the inflation: not enough

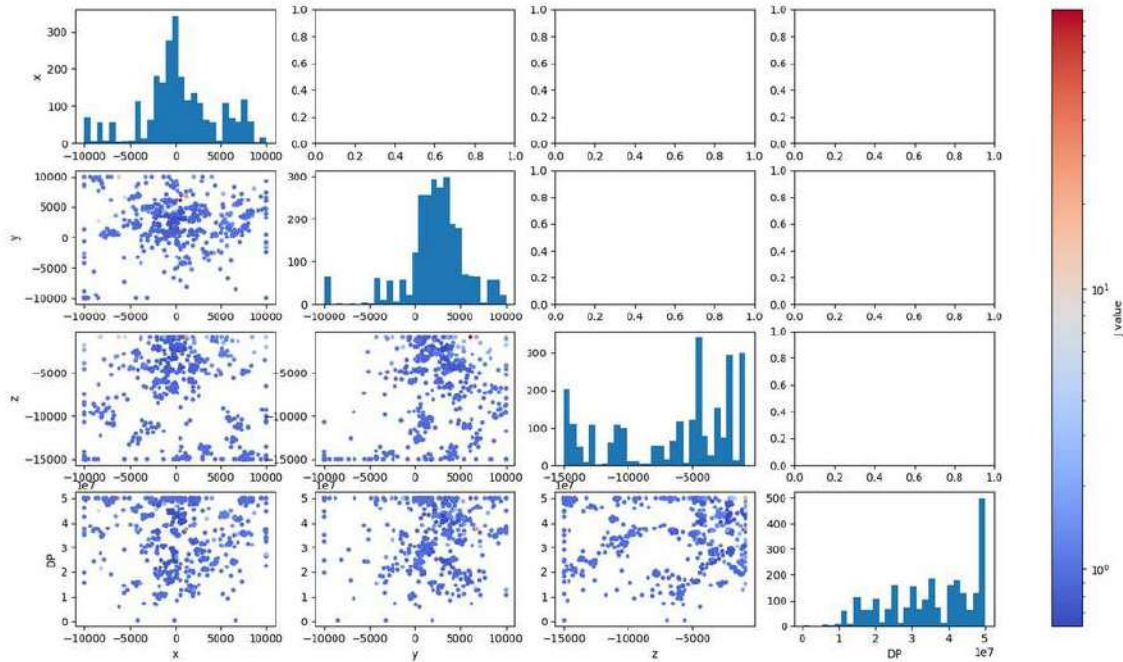


Figure 1.9: Distribution of the evaluation point within the search space. The diagonal shows the frequency of the evaluation for each parameter $x, y, z, \Delta P$. Below are slices of the search space showing the localization of the search points. More points mean that the solution is more likely to be here, because this is where the algorithm takes the most time to converge.

Parameters	2011-2014 inflation source	2010 deflation source
Model	Numerical	Analytical
Geometry	Sphere	Point
Center latitude (deg)	63.648,	63.655
Center longitude (deg)	19.610	-19.619
Depth (km)	2.2	2.5 to 2.8
Volume change ($10^6 m^3$)	5.7	3.7 to 4.1
Radius (km)	0.8	X

Table 1.1: Comparison of the parameters of the 2011-2014 inflation source and the 2010 deflation source responsible for the April peak. Note that the values for the analytical models are intervals because they are the 95 % confidence intervals resulting from the Bayesian inversion. In terms of horizontal position, the extents overlap for the 3 models. However, the depths are different between the 2011-2015 and the 2010 source. This may be due to the different geometry of the modeled source. The volume changes are consistent for both models of the 2011-2014 source.

magma was present to reach the critical pressure that could have triggered the opening of the chamber. Of course, more tests and uncertainty quantification on our models would make this conclusion more certain.

1.5 Limits and perspectives

In this first chapter, we have implemented parametric optimization based on numerical models, a method already used in the volcano geodesy community in a transparent and open-source way. In this respect, the `eyjaFEM` code can be easily extended, modified and plugged in to tackle other problems.

The pipeline was initially designed for the case of the Eyjafjallajökull 2011-2015 inflation, but can be easily extended to other volcanic events by simply changing the input files for the [DEM](#) and the InSAR and GNSS data. For the particular 2011-2015 inflation, the results obtained were convincing and consistent with what was expected: the inflating source is likely to be the same as the one responsible for the May 2010 summit eruption reported by Freysteinn Sigmundsson, Hreinsdóttir, et al. [2010](#).

Nevertheless, further tests and optimization procedures should be performed to give more credibility to this result. First, it would be interesting to inverse for a flattened spheroidal source instead of a sphere, as it is closer in shape to the [sill](#) expected under the volcano. In fact, [ibid.](#) mention a "complex network of interconnected sills" and invert assuming such a shape. In practice, few changes to the code would be required, as the ellipsoidal surface is easily defined in GMSH. The issue that would be raised is more on the increasing dimensionality of the problem, even by fixing ΔP as we fixed R_s , the model parameter would be $p = (a, b, c, x, y, z) \in \mathbb{R}^6$ where a, b, c are the half-axes of the ellipsoid.

Another important issue to address is the uncertainty of the result given by the optimization procedure. This is a drawback of conventional global optimization, as reported by Van Stein et al. [2018](#), is the lack of a confidence interval on the optimized parameters p_{opt} . Some approximate methods rely on the Hessian (Menke [2012](#)) in this respect, but nothing is as satisfying as the probability distribution for each parameter computed by the method of Bagnardi and Andrew Hooper [2018](#).

Moreover, we chose to use derivative-free solvers, whereas a derivative $J'(p)$ could actually be formally derived using sensitivity analysis theory. The computation of such a derivative over the mesh is achievable with partial differential equation (PDE)-based FEM codes such as FreeFEM++, which can solve any variational formulation of elliptic PDE over a given mesh (Hecht [2012](#)). This would require a change in the FEM solver of `eyjaFEM`, which is possible thanks to the modularity of the code.

Apart from the 2011-2015 inflation event, future studies should focus on the other movements we have reported at Eyjafjallajökull. The following deflation could be of interest, especially because it could influence the volcanic activity at Katla, as studied by Albino and F. Sigmundsson [2014](#). The potential [dike](#) intrusion shown by the linear pattern of CSK A32 interferograms also needs to be verified and could be confirmed or infirmed with seismic data for this period.

As shown in figure [A6](#), the following deflation is also of interest. It would be valuable to study it to assess its parameters, and also to understand its causes: what happened then? Does the magma cooled down, causing contraction and deflation, or did it move away, transported in the neighbouring Katla volcano?

Although the presented approach has some limitations, we hope that the code implemented will be improved and reused. By enriching the numerical models, a step forward could be made for hazard assessment and understanding of magmatic systems in general.

2

Level-set shape optimization applied to magma domain inversion

2.1 Presentation

Another major part of the work done at the Institute of Earth Sciences was the adaptation of shape optimization, a method developed as a tool in engineering, to the inverse problem of volcano geodesy. After hesitation and many unsuccessful attempts, a good paradigm was chosen and the adaptation showed first results. Since it has never been reported in the field of volcano geodesy, we decided to write an article to present the approach to researchers in the field. The article is co-written with my supervisor, Freysteinn Sigmundsson, and the method has been adapted with advice from Charles Dapogny. Below is a draft version of the paper, still at the preprint stage.



Figure 2.1: Bjarnmarsteinn, in Breiðafjördur. Old magmatic reservoir apparent at the surface after differential erosion of the host rock. The basaltic columns indicates that the cooling was slow and progressive. This is part of the structures we are trying to model below.

2.2 Article

1 Shape optimization for improved

2 understanding of magmatic plumbing

3 systems

4 Théo Perrot, Freysteinn Sigmundsson
5 June 2024

6 Abstract

7 In volcano geodesy, inverse problems caused by identifying the location and
8 shape of magmatic bodies based on ground deformation data are common.
9 Traditional approaches often rely on models with predefined shapes, which
10 can limit their accuracy. To address this, we present a shape optimisation
11 method using a level-set approach that flexibly determines the optimal
12 shape of a magma chamber without prior shape assumptions. By minimising
13 the discrepancy between observed and modelled surface displacements,
14 our adapted algorithm becomes suitable for solving inverse volcano deforma-
15 tion problems. We explore the capabilities of this approach with synthetic
16 data and apply it to InSAR observations of the Svatsegi volcanic system in
17 Iceland, demonstrating its potential to improve volcanic hazard assessment
18 after maturation through future work.

19 1 Introduction

20 1.1 Challenge

21 In volcano geodesy, inverse problems are central to estimating the position
22 of magmatic bodies using ground motion as a proxy. Displacement is ob-
23 served by geodetic measurements such as Global Navigation Satellite System
24 (GNSS) point positioning, leveling campaigns, or Synthetic Aperture Radar
25 (InSAR) interferometry within a volcanic field, and the subsurface processes
26 causing the movement are inferred from these observations (Dzurisin 2007).
27 Magmatic sources are modeled as pressurized cavities that deform the sur-
28 rounding host rocks and cause the surface to move. Various inversion meth-
29 ods based on parametric analytical or numerical models aim at finding the
30 optimal values for the vector of d free parameters $\vec{m} \in \mathbb{R}^d$ of the model. Then
31 an error function $J(\vec{m})$ is representative of the misfit between the observed
32 displacements and the prediction of the model. \vec{m}_{opt} can then be found using
33 various inversion techniques that minimize J : global optimization based on
34 analytic (Cervelli et al. 2001) or numerical models (Hickey and Gottsmann
35 2014, Charco and Galán del Sastre 2014), Bayesian inference (Bagnardi and
36 Hooper 2018, Trasatti 2022), or genetic algorithms (Velez et al. 2011) on
37 analytic models. The choice of the method is constrained by the reasonable
38 number of evaluations of $J(\vec{m})$: numerical models handle a complex descrip-
39 tion of the system, but are computationally expensive compared to analytic
40 models, which on the other hand may lead to an oversimplification (Taylor,
41 Johnson, and Herd 2021).

42 However, each of these finite-dimensional optimization methods is limited
43 by the intrinsic assumption of a definite parametric shape for the source. In
44 fact, analytic expressions can be derived for only a few regular shapes such as
45 point source (Mogi 1958), finite sphere source (McTigue 1987), or ellipsoidal
46 source (Yang, Davis, and Dieterich 1988), and any numerically generated
47 shape must be parameterized to be inverted. Even in the case where complex
48 shapes are chosen, they would require additional describing parameters, and
49 ultimately any of the above methods may face the curse of dimensionality.
50 The goal of this paper is not to give a definitive answer to these limitations,
51 but rather to lay the first stone for a new approach that overcomes these
52 difficulties.

53 1.2 Shape optimization

54 Shape (and topology) optimization aims to find the shape that minimizes a
55 given function defined on a given system, without the need for prior assump-

⁵⁶ tions about shape and topology. It is actively developed by part of the applied
⁵⁷ mathematics community and is widely used in engineering to find optimal
⁵⁸ designs for systems: In structural mechanics, to maximize the stiffness of a
⁵⁹ solid structure such as a cantilever beam (Bendsøe and Ole Sigmund 2004),
⁶⁰ in fluid-structure interaction on heat exchangers or flying obstacles (F. Feppon et al. 2020), and even as a way to explore new architecture for buildings
⁶¹ (Beghini et al. 2014). Most finite element simulation and design software now
⁶² implements an embedded shape optimization module (Frei 2015, Slavov and
⁶³ Konsulova-Bakalova 2019, Le Quilliec 2014). However, its use has not yet
⁶⁴ been reported in the context of inverse problems in volcano geodesy, where
⁶⁵ it can overcome the shape hypothesis problem as long as an internal pressure
⁶⁶ value is assumed.

⁶⁷ Many paradigms coexist in shape optimization as reviewed by Ole Sigmund and Maute 2013, one of the most popular being SIMP optimization,
⁶⁸ where a density value is optimized for each element of the mesh with values
⁶⁹ between 0 (void) and 1 (material) before being black and white filtered to
⁷⁰ output a design (O. Sigmund 2001, Bendsøe and Ole Sigmund 2004), with
⁷¹ several open source implementations (Andreassen et al. 2011, Hunter et al.
⁷² 2017). We chose level-set shape optimization instead because it has the ad-
⁷³ vantage of providing an explicit representation of the boundary at each step
⁷⁴ of the optimization, which is crucial for us as explained later (section 2). For
⁷⁵ this, we relied on the work of Dapogny and Florian Feppon 2023, who thor-
⁷⁶oughly described and vulgarized the method, as well as providing a freely
⁷⁷ available open source implementation of the method, `sotuto` (Dapogny and
⁷⁸ Florian Feppon 2024), which we modified and extended to adapt it to inverse
⁷⁹ geodetic problems.

⁸⁰ 2 Method

⁸¹ Here we briefly present the key ingredients of level set shape optimization
⁸² along with their implications for our problem. The full mathematical back-
⁸³ ground on which it relies is not detailed, but see this chapter by Allaire,
⁸⁴ Dapogny, and Jouve 2021 for a comprehensive step-by-step description sup-
⁸⁵ported by proofs and theorems. It is also worth noting that many aspects
⁸⁶ of secondary importance to the method are not mentioned for the sake of
⁸⁷ brevity. For the unfamiliar reader interested in understanding the method,
⁸⁸ the lecture (especially part III) given by Dapogny and Bonnetier 2024 at the
⁸⁹ Université Grenoble Alpes is also recommended.

⁹² **2.1 Model**

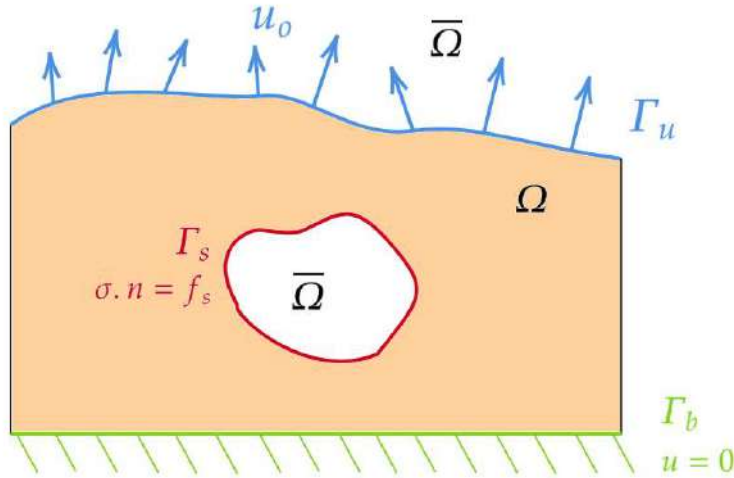


Figure 1: 2D sketch of the problem. The optimized boundary (where the level-set function is zero) is the magma chamber wall Γ_s subjected to a uniform normal load $\sigma(u).n = f_s$ on Γ_s , where $f_s = -\Delta P.n$, where n is the unit normal vector and ΔP is the pressure change between the magma source and the surrounding crust. The bottom surface Γ_b is fixed ($u = 0$). The other boundaries are free. The target displacement field u_o is known on the upper surface Γ_u .

⁹³ Let Ω be a bounded domain of \mathbb{R}^3 whose shape we want to optimize
⁹⁴ by modifying parts of its boundary $\partial\Omega$. As for classical analytical mod-
⁹⁵ els of volcanic deformation induced by magmatic activity, Ω is a domain
⁹⁶ representing a portion of the shallow Earth crust, including the volcano, as-
⁹⁷ sumed to be homogeneous, isotropic, and elastic. The governing equations
⁹⁸ are $-\operatorname{div}(Ae(u)) = 0$ in Ω , where $e(u)$ is the strain tensor of the displacement
⁹⁹ field u and A is the constitutive law tensor, $Ae = 2\mu e + \lambda \operatorname{tr}(e)\operatorname{Id}$ for linear
¹⁰⁰ elasticity. Boundaries under different conditions, see Fig. 1 for all notations.

¹⁰¹ The part of $\partial\Omega$ to be optimized is Γ_s , the boundary magma chamber,
¹⁰² which is modeled as an empty, uniformly pressurized cavity. Therefore, a
¹⁰³ value for the internal pressure ΔP must be assumed (see Discussion for devel-
¹⁰⁴ opment). In the following text we talk about optimizing $\partial\Omega$, but in practice

¹⁰⁵ only $\Gamma_s \subset \partial\Omega$ is of interest and will be modified, any other boundary will be
¹⁰⁶ fixed during the iterations.

¹⁰⁷ We want to find $\partial\Omega$ such that the displacement of the model $u(\Omega)$ is as
¹⁰⁸ close as possible to the observed displacement u_o on the surface Γ_u . Thus,
¹⁰⁹ the unconstrained shape optimization problem we want to solve is the mini-
¹¹⁰ mization of a squared RMS discrepancy

$$\min_{\Omega} J(\Omega) = \int_{\Gamma_u} (u(\Omega) - u_o)^2 dS \quad (1)$$

¹¹¹ 2.2 Hadamard Boundary Variation

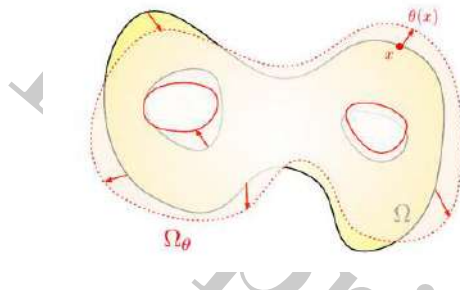


Figure 2: Reproduced from Allaire, Dapogny, and Jouve 2021

¹¹² Overall, this method can be considered a classical iterative gradient de-
¹¹³ scent algorithm. J is first initialized at J_0 with an instructed first guess
¹¹⁴ for Ω_0 and then iteratively decreased by moving $\partial\Omega$ of a given step in a
¹¹⁵ given descent direction $\theta : \mathbb{R}^3 \mapsto \mathbb{R}^3 \in W^{1,\inf}$ (the Sobolev space of uni-
¹¹⁶ formly bounded functions, Allaire, Dapogny, and Jouve 2021) chosen using
¹¹⁷ the shape derivative $J'(\Omega)(\theta)$.

¹¹⁸ The boundary variation method of Hadamard 1908 introduces the notion
¹¹⁹ of shape differentiation $F'(\Omega)(\theta)$ of a functional F defined on Ω in the di-
¹²⁰ rection θ . In short, such a derivative is based on the variation of a bounded
¹²¹ domain $\Omega \mapsto \Omega_\theta := (Id + \theta)(\Omega)$: the surface $\partial\Omega$ is slightly moved according
¹²² to a small vector field $\theta(x)$, as shown in Fig. 2. Once such a derivative
¹²³ exists, one can compute a descending direction at the n^{th} step θ_n , such as
¹²⁴ $J'(\Omega)(\theta_n) \leq 0$, so $J_{n+1} \leq J_n$, to decrease the value of J at each iteration.

¹²⁵ In our case, after derivation based on the Cea 1986 formal method, we
¹²⁶ found under the variational form :

$$J'(\Omega)(\theta) = \int_{\Gamma_s} \left(Ae(u) : e(p) + \frac{\partial f_s}{\partial n} p + \frac{\partial p}{\partial n} f_s + \kappa f_s p \right) \cdot \theta \cdot ndS \quad (2)$$

¹²⁷ where $\kappa = \operatorname{div}(n)$ is the mean curvature at the boundary, and p is the
¹²⁸ adjoint solution of

$$\forall v \in H^1(\mathbb{R}^3), \int_{\Gamma_u} 2(u_\Omega - u_o)v dS + \int_{\Omega} Ae(v) : e(p) dV = 0 \quad (3)$$

and $p = 0$ on Γ_b

¹²⁹ From there, we can trivially move Ω in the direction $\theta = -A$ (where
¹³⁰ A is the integrand term in parentheses) to ensure that $J'(\Omega)(\theta) \leq 0$. This
¹³¹ guarantees that $J(\Omega_{n+1}) \leq J(\Omega_n)$: the series $J(\Omega_n)$ converges to a minimum.

¹³² 2.3 Level-set representation

¹³³ A key issue is the representation of the surface to be optimized. The level
¹³⁴ set method allows to track dramatic changes as well as topology variations
¹³⁵ (creation of new holes). A certain function $\phi : D \mapsto \mathbb{R}$ is defined over the
¹³⁶ domain $D \in \mathbb{R}^3$ in such a way that the shape boundary is the level set 0,
¹³⁷ i.e. reads $\partial\Omega = \phi(x = 0)$. Basically, ϕ can be taken as the signed distance
¹³⁸ between any point x and $\partial\Omega$, as shown in the example fig. 3. In this way,
¹³⁹ $\partial\Omega$ is implicitly manipulated when transforming ϕ .

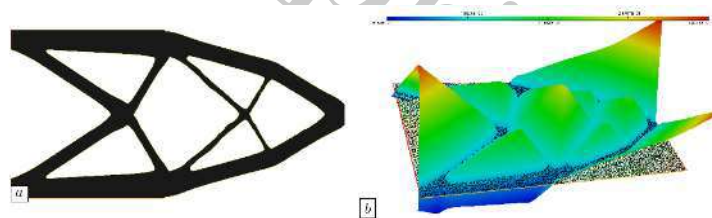


Figure 3: Reproduced from Dapogny and Florian Feppon 2023

¹⁴⁰ Ω_n is then deformed by advecting the corresponding ϕ_n with a velocity
¹⁴¹ field $V(x) = \tau_n \theta_n$, where τ_n is the additional step size. The advection equa-
¹⁴² tion usually appears in fluid mechanics to describe the evolution of a quantity
¹⁴³ transported by a given velocity field, but here there is a smooth and flexible
¹⁴⁴ way to modify ϕ which ensures smoothness of Ω_{n+1} and change of topology
¹⁴⁵ (see Allaire, Dapogny, and Jouve 2021).

¹⁴⁶ 2.4 Numerical implementation

¹⁴⁷ In practice, the D domain is discretized into a mesh T_n on which each vari-
¹⁴⁸ ational form is solved at each iteration n . This includes the solution of the

¹⁴⁹ elasticity to get u_n , the adjoint state p_n , the computation of the shape gradient J'_n , the descent direction θ_n , the advection of ϕ_n . In **sotuto** it is achieved
¹⁵⁰ by calling scripts written in FreeFem++, a finite element software that allows
¹⁵¹ solving any integral form of elliptic PDE (Hecht 2012).
¹⁵²

¹⁵³ Once the new form Ω_{n+1} is computed and discretized thanks to a local
¹⁵⁴ remeshing phase, a new evaluation of J^{n+1} is performed. Since τ is arbitrarily
¹⁵⁵ fixed and initialized to 1, it can happen that Ω_n is shifted by too large a step
¹⁵⁶ and so $J_{n+1} \geq J_n$. To adjust the step size, a line search procedure is
¹⁵⁷ implemented and adjusts the step size by decreasing it if the new iteration
¹⁵⁸ is the worst to ensure an improvement of J by computing a new Ω_{n+1} being
¹⁵⁹ a less deformed version of Ω_n . On the contrary, if Ω_{n+1} is accepted, τ is
¹⁶⁰ increased to speed up convergence. A tolerance is set to accept iterations if
¹⁶¹ the increase in J is reasonable.

¹⁶² The global optimization loop has no termination criterion. Thus, it is up
¹⁶³ to the user to stop it when no significant improvement in J can be achieved,
¹⁶⁴ or when the shape is not realistic.

¹⁶⁵ The loop and the line search are implemented in Python in **sotuto**. Then
¹⁶⁶ the FreeFem scripts are called by the Python script core and data is ex-
¹⁶⁷ changed via temporary files.

¹⁶⁸ The above aspects are implemented in **sotuto**. However, we extended its
¹⁶⁹ functionality to handle our geophysical problem, in a fork we called **magmaOpt**.
¹⁷⁰ This included: scripts to create the domain and initial source with a flexible
¹⁷¹ mesher GMSH which handle complex geometries such as the one generated
¹⁷² by topography Geuzaine, Remacle, and Dular 2009 ,adapting FreeFem scripts
¹⁷³ to different error functions, allowing optimization of the loaded boundary Γ_s
¹⁷⁴ and so on.

¹⁷⁵ 3 Validation with synthetic data

¹⁷⁶ To test the method, the idea is to do a kind of cross-validation. On the
¹⁷⁷ one hand, we form synthetic observation data from a known source. On
¹⁷⁸ the other hand, we initialized the algorithm with a first guess for the source
¹⁷⁹ shape and location. We expect the algorithm to iteratively modify the shape
¹⁸⁰ of the source and converge to the correct shape and location. In fact, the
¹⁸¹ 3D location of the source (e.g., its center of gravity for a random shape) is
¹⁸² not directly optimized as a vector of discrete parameters, but is modified by
¹⁸³ the simple fact that the boundary is free to move in any direction, and thus
¹⁸⁴ can take on a kind of "average rigid body motion" as it gradually moves the
¹⁸⁵ center in a given direction.

¹⁸⁶ In practice, the synthetic observed surface displacement field is derived

¹⁸⁷ from the McTigue 1987 solution, an analytical approximation of the displacement caused by a uniformly pressurized spherical cavity (the magma domain) embedded in an isotropic, homogeneous, and planar elastic medium (the host crust) with elastic constants $t_p E = 10\text{GPa}$ and $\mu = 0.25$.

¹⁹¹ Usually, the quantities to be determined with parametric inversion based on a McTigue model are the location and the radius. The pressure change can also be left as a free parameter, but is interchangeable with the radius, so one must be fixed to determine the other, see (Greiner 2021) for more details. For the synthetic source, we fixed these free parameters to $z = -5\text{km}$, $\Delta P = 10\text{MPa}$, $R = 1.5\text{km}$, which are typical values for inverted magmatic domains.

¹⁹⁸ `magmaOpt` is then allowed to run freely, without any termination condition, to see whether or not it succeeds in converging from the ellipsoid to the ¹⁹⁹ McTigue sphere we used to generate the synthetic displacement.

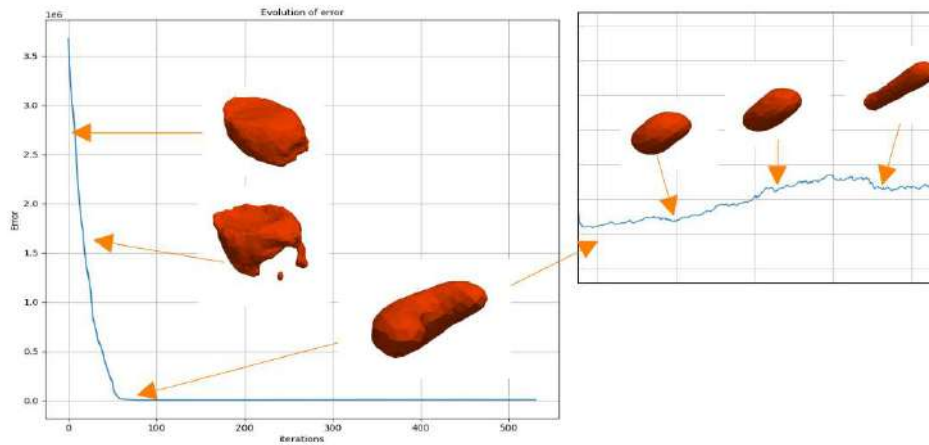


Figure 4: Evolution of error and successive shapes taken by the magma source during an optimization loop. The initial guess is a flat ellipsoid of semi-axes $r_x = 2\text{km}$, $r_y = 3\text{km}$, $r_z = 1\text{km}$ centered on the true spherical source. The minimum is reached at iteration 82.

²⁰¹ As shown in the figure 4, the algorithm seems to converge to a minimum. ²⁰² After that, the slope of the cost function is positive because a small increase ²⁰³ in J is allowed. It is obvious that no other minima are found, as the shape ²⁰⁴ evolves towards a stick-shaped feature, far from the expected solution. We ²⁰⁵ can also discuss the minima found. The surface reached is obviously not a

²⁰⁶ sphere, but it is closer than any shape found before. We expect the shape to
²⁰⁷ be closer to a sphere with a finer mesh defined. Many improvements could be
²⁰⁸ realized: for example, once it is obvious that the algorithm will not converge
²⁰⁹ to a better solution, we could restart the algorithm on the best solution
²¹⁰ found, set new evolution parameters, and allow a finer mesh. By repeating
²¹¹ this process automatically, it may be possible to arrive at a more likely shape
²¹² for the magma reservoir.

²¹³ 4 Real test case : Svartsengi 2022 inflation

²¹⁴ We now apply the method to infer the shape of a magma domain in a recent
²¹⁵ period of volcanic unrest and eruption in SW Iceland by evaluating the shape
²¹⁶ of a magma body responsible for the ground inflation observed from 21 April
²¹⁷ to 14 June 2022 at Svartsengi on the Reykjanes peninsula. This is one of
²¹⁸ 5 inflation episodes that preceded catastrophic dike breaches and eruptions
²¹⁹ at the Sundhnúkur crater row, which caused the destruction of the city of
²²⁰ Grindavík (Sigmundsson et al. 2024).

²²¹ The observational data used are the line-of-sight (LOS) displacement
²²² maps of the area from Cosmo SkyMed available in Parks et al. 2024, the
²²³ data used in Sigmundsson et al. 2024. After uniform downsampling and
²²⁴ mesh reprojection (the data points must be aligned on the mesh nodes), the
²²⁵ ascending A32 and descending D132 tracks were both used in the RMS error
²²⁶ function we adapted to the LOS geometry.

$$J(\Omega) = \sum_{i \in tck} \alpha_i \int_{\Gamma_u} (L_i(u(x)) - l_o^i(x))^2 dS \quad (4)$$

²²⁷ Where $tck = \{A125, D132\}$. For each track i , α_i is the weight of the track
²²⁸ ($\forall i, \alpha_i = 1$ here), $L_i : \mathbb{R}^3 \mapsto \mathbb{R}$ is the function that projects the 3D sur-
²²⁹ face displacement given by the model into the LOS geometry, and l_o^i is the
²³⁰ observed LOS displacement.

²³¹ We then used the framework developed above, only projecting the InSAR
²³² data onto the mesh of D and modifying the expression of the error function
²³³ in `magmaOpt`.

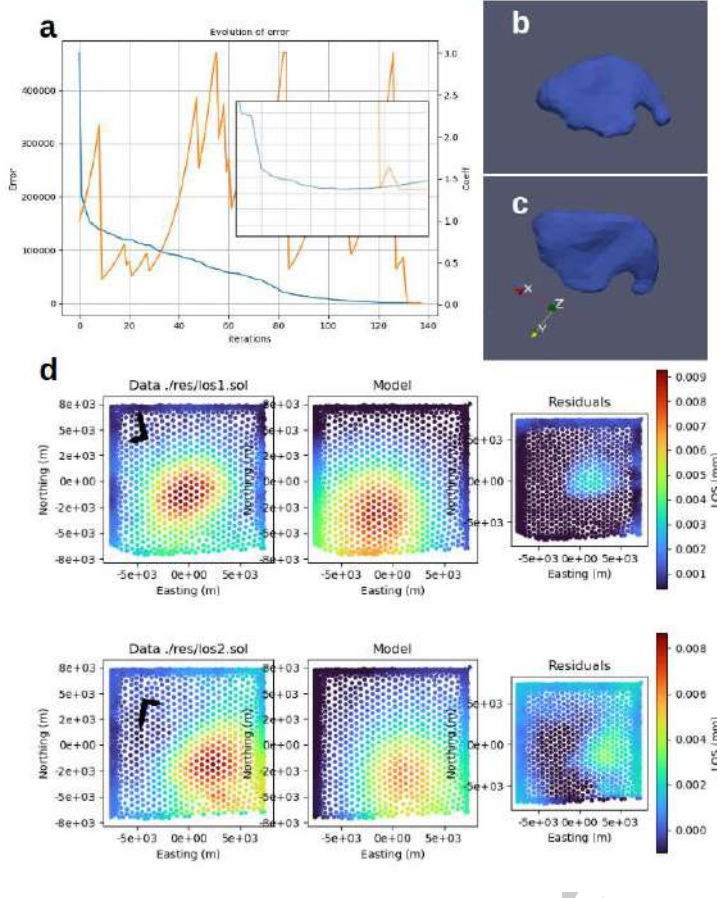


Figure 5: a) Convergence plot with embedded zoom. The blue line is the error and the orange line is the evolution of τ . Minima are reached at iteration 128. b,c) Side and top view of the source Γ_s minimizing J . d) Data, model and residuals of the LOS displacements at iteration 128 for the two InSAR tracks A32 (top) and D132 (bottom). Black arrows are heading and looking directions, coordinates are ISN16 **islands** shifted to a local origin (2529373E, 179745N).

234 The results shown in figure 5 are encouraging: after providing an initial
 235 guess located at the center of inflation at depth for a sphere of radius RR,
 236 the algorithm is able to iteratively change the shape and depth of the magma
 237 domain to finally result in a sill-like flattened spheroid whose centroid is lo-
 238 cated at DD depth. This is consistent with the presumed depth found in
 239 the supporting information of Sigmundsson et al. 2024, which performs an

²⁴⁰ analytical model-based inversion. Although the pressure must be fixed, as
²⁴¹ explained in 1.2, the result can be used to compare the final shape of the
²⁴² magmatic intrusion and give a richer insight into it. Here we see interesting
²⁴³ features, such as an increasing thickness on the north side, that can't
²⁴⁴ be traced by any other method. The algorithm produces features that we
²⁴⁵ consider to be artifacts, probably due to mesh refinement problems, such as
²⁴⁶ small holes or horn-shaped features.

²⁴⁷ 5 Discussion

²⁴⁸ This work paves the way for a new class of methods that tackle an unknown
²⁴⁹ geometry of the magmatic domains, thus giving the possibility to explore
²⁵⁰ irregular shapes that are more likely to exist compared to any other usually
²⁵¹ assumed regular shapes. However, even if the first results presented are
²⁵² promising, many questions remain to be answered. First of all, the internal
²⁵³ pressure of the chamber must be specified, which is a strong hypothesis.
²⁵⁴ In this context, the precise shape of the source should be determined as a
²⁵⁵ second step. The traditional analytical model-based inversion would be run
²⁵⁶ first, giving a pressure and a first educated guess for the position and shape
²⁵⁷ of Ω_0 . Then a more realistic shape could be sought with a shape optimization
²⁵⁸ taking the output of the inversion as an initial guess.

²⁵⁹ Adding constraints may also be an interesting way to explore. For ex-
²⁶⁰ ample, the volume of the source could be constrained to be within bounds
²⁶¹ or even to match a certain value. The implemented shape optimization is
²⁶² certainly able to handle constraints as described by **allaire202**. The physical
²⁶³ meaning of the best shape might benefit from a more constrained problem,
²⁶⁴ and the less influencing deeper part of the source might be less random.

²⁶⁵ To better understand the influence of data partitioning and variablitiy,
²⁶⁶ additional tests could be run with synthetic data. We can think of tests
²⁶⁷ such as masking part of the surface displacement field, introducing noise
²⁶⁸ and parasitic signals, reducing the number of data points, as is often the
²⁶⁹ case in reality with areas of volcanic systems lacking data coverage (glacier,
²⁷⁰ river, lava, forest) and subjected to perturbations (atmospheric distortion,
²⁷¹ weather).

²⁷² It is also important to mention that the behavior of the algorithm is
²⁷³ influenced by numerous parameters of varying importance, starting from the
²⁷⁴ discretization length (element size) or the domain extent, to the limits of the
²⁷⁵ step size τ , the regularization length, or the number of iterations allowed by
²⁷⁶ the line search. A systematic study of each of these parameters would be
²⁷⁷ beneficial in assessing the quality of the shape inferred.

²⁷⁸ Exploring a way to quantify the uncertainty of the answer is also crucial.
²⁷⁹ For example, a sensitivity analysis approach could be considered, as well as
²⁸⁰ the inclusion of a probabilistic quantity.

²⁸¹ 6 Conclusion

²⁸² The present study has successfully demonstrated the application of inverse
²⁸³ problems and computational methods to infer the shape of a magma domain
²⁸⁴ beneath a volcano using ground inflation data from satellite observations.
²⁸⁵ The shape optimization technique used in this research showed a new way to
²⁸⁶ identify the most likely shape of the magma chamber. It was intended as an
²⁸⁷ opening to new methods rather than a complete solution.

²⁸⁸ We have shown that modifying a shape optimization algorithm to handle
²⁸⁹ geophysical problems is feasible and of interest. Tests on synthetic data
²⁹⁰ showed to some extent the relevance of the approach, although the best
²⁹¹ sources found exposed the limitations faced by these first attempts of shape
²⁹² optimization for volcano geodesy. The test on real data showed a concrete
²⁹³ case of how the method could be used after being more mature.

²⁹⁴ The perspectives are numerous. The numerical nature of the models
²⁹⁵ allows to easily add complexities to the modeling, such as complex mechanical
²⁹⁶ behavior of the crust (plaxticity, viscoelasticity, poroelsaticity), additional
²⁹⁷ loads (tectonic stress, tidal loads, glacier weights), or inhomogeneities. We
²⁹⁸ hope that the open source code `magmaOpt` developed by us will be modified
²⁹⁹ and extended by future work.

³⁰⁰ By addressing these limitations and extending this approach, researchers
³⁰¹ can further improve the accuracy and reliability of magma domain shape
³⁰² inference. Ultimately, the development of more sophisticated models will
³⁰³ enable geophysicists to better monitor volcanic activity, predict eruptions,
³⁰⁴ and provide critical support for hazard mitigation strategies.

³⁰⁵ References

- ³⁰⁶ Allaire, Grégoire, Charles Dapogny, and François Jouve (2021). “Chapter 1
³⁰⁷ - Shape and Topology Optimization”. In: *Geometric Partial Differential
308 Equations - Part II*. Ed. by Andrea Bonito and Ricardo H. Nochetto.
³⁰⁹ Vol. 22. Handbook of Numerical Analysis. Elsevier, pp. 1–132. DOI: 10.
³¹⁰ 1016/bs.hna.2020.10.004. URL: <https://www.sciencedirect.com/science/article/pii/S1570865920300181>.

- 312 Andreassen, Erik et al. (Jan. 2011). "Efficient Topology Optimization in
313 MATLAB Using 88 Lines of Code". In: *Structural and Multidisciplinary*
314 *Optimization* 43.1, pp. 1–16. ISSN: 1615-147X, 1615-1488. DOI: 10.1007/
315 s00158-010-0594-7. URL: <http://link.springer.com/10.1007/s00158-010-0594-7> (visited on 08/22/2024).
- 316
- 317 Bagnardi, Marco and Andrew Hooper (July 2018). "Inversion of Surface De-
318 formation Data for Rapid Estimates of Source Parameters and Uncer-
319 tainties: A Bayesian Approach". In: *Geochemistry, Geophysics, Geosys-*
320 *tems* 19.7, pp. 2194–2211. ISSN: 1525-2027, 1525-2027. DOI: 10.1029/
321 2018GC007585. URL: <https://agupubs.onlinelibrary.wiley.com/doi/10.1029/2018GC007585> (visited on 02/29/2024).
- 322
- 323 Beghini, Lauren L. et al. (Feb. 1, 2014). "Connecting Architecture and En-
324 gineering through Structural Topology Optimization". In: *Engineering*
325 *Structures* 59, pp. 716–726. ISSN: 0141-0296. DOI: 10.1016/j.engstruct.
326 2013.10.032. URL: <https://www.sciencedirect.com/science/article/pii/S0141029613005014> (visited on 08/21/2024).
- 327
- 328 Bendsøe, Martin P. and Ole Sigmund (2004). "Topology Optimization by
329 Distribution of Isotropic Material". In: *Topology Optimization: Theory,*
330 *Methods, and Applications*. Ed. by Martin P. Bendsøe and Ole Sigmund.
331 Berlin, Heidelberg: Springer, pp. 1–69. ISBN: 978-3-662-05086-6. DOI: 10.
332 1007/978-3-662-05086-6_1. URL: https://doi.org/10.1007/978-3-662-05086-6_1 (visited on 08/21/2024).
- 333
- 334 Cea, Jean (1986). "Conception Optimale Ou Identification de Formes, Calcul
335 Rapide de La Dérivée Directionnelle de La Fonction Coût". In: *ESAIM:*
336 *Modélisation mathématique et analyse numérique* 20.3, pp. 371–402. ISSN:
337 1290-3841. URL: http://www.numdam.org/item/M2AN_1986__20_3_371_0/ (visited on 08/22/2024).
- 338
- 339 Cervelli, P. et al. (2001). "Estimating Source Parameters from Deformation
340 Data, with an Application to the March 1997 Earthquake Swarm off the
341 Izu Peninsula, Japan". In: *Journal of Geophysical Research: Solid Earth*
342 106.B6, pp. 11217–11237. ISSN: 2156-2202. DOI: 10.1029/2000JB900399.
343 URL: <https://onlinelibrary.wiley.com/doi/abs/10.1029/2000JB900399>
344 (visited on 08/22/2024).
- 345
- 346 Charco, M. and P. Galán del Sastre (Mar. 1, 2014). "Efficient Inversion of
347 Three-Dimensional Finite Element Models of Volcano Deformation". In:
348 *Geophysical Journal International* 196.3, pp. 1441–1454. ISSN: 0956-540X.
349 DOI: 10.1093/gji/ggt490. URL: <https://doi.org/10.1093/gji/ggt490> (visited on 08/22/2024).
- 349
- 350 Dapogny, Charles and Eric Bonnetier (2024). *An Introduction to Shape and*
351 *Topology Optimization*. URL: <https://membres-ljk.imag.fr/Charles.Dapogny/coursoptim.html> (visited on 08/21/2024).
- 352

- 353 Dapogny, Charles and Florian Feppon (Oct. 31, 2023). “Shape Optimization
354 Using a Level Set Based Mesh Evolution Method: An Overview and
355 Tutorial”. In: *Comptes Rendus. Mathématique* 361.G8, pp. 1267–1332.
356 ISSN: 1778-3569. DOI: 10.5802/crmath.498. URL: <https://comptes-rendus.academie-sciences.fr/mathematique/articles/10.5802/crmath.498/> (visited on 08/02/2024).
- 357 — (July 30, 2024). *Dapogny/Sotuto*. URL: <https://github.com/dapogny/sotuto> (visited on 08/21/2024).
- 358 Dzurisin, Daniel (2007). *Volcano Deformation: Geodetic Monitoring Techniques*. Springer-Praxis Books in Geophysical Sciences. Berlin ; New York : Chichester, UK: Springer ; Praxis. 441 pp. ISBN: 978-3-540-42642-4.
- 359 Feppon, F. et al. (Sept. 15, 2020). “Topology Optimization of Thermal Fluid–Structure
360 Systems Using Body-Fitted Meshes and Parallel Computing”. In: *Journal of Computational Physics* 417, p. 109574. ISSN: 0021-9991. DOI: 10.1016/j.jcp.2020.109574. URL: <https://www.sciencedirect.com/science/article/pii/S002199912030348X> (visited on 08/22/2024).
- 361 Frei, Walter (Dec. 29, 2015). *Designing New Structures with Shape Optimization*. COMSOL. URL: <https://www.comsol.com/blogs/designing-new-structures-with-shape-optimization> (visited on 08/22/2024).
- 362 Geuzaine, Christophe, Jean-Francois Remacle, and P Dular (2009). “Gmsh: A Three-Dimensional Finite Element Mesh Generator”. In: *International Journal for Numerical Methods in Engineering* 79.11, pp. 1309–1331.
- 363 Greiner, Sonja HM (2021). “Including Topography and a 3D-elastic Structure into a Finite-Element Deformation Model of Grímsvötn, Iceland”. PhD thesis. URL: <http://hdl.handle.net/1946/38435>.
- 364 Hadamard, J. (1908). *Mémoire Sur Le Problème d’analyse Relatif a l’équilibre Des Plaques Élastiques Encastrees*. Académie Des Sciences. Mémoires. Imprimerie nationale. URL: <https://books.google.co.ma/books?id=8wSUMAEACAAJ>.
- 365 Hecht, F. (2012). “New Development in FreeFem++”. In: *Journal of Numerical Mathematics* 20.3-4, pp. 251–265. ISSN: 1570-2820. URL: <https://freefem.org/>.
- 366 Hickey, James and Joachim Gottsmann (June 2014). “Benchmarking and Developing Numerical Finite Element Models of Volcanic Deformation”. In: *Journal of Volcanology and Geothermal Research* 280, pp. 126–130. ISSN: 03770273. DOI: 10.1016/j.jvolgeores.2014.05.011. URL: <https://linkinghub.elsevier.com/retrieve/pii/S037702731400153X> (visited on 02/29/2024).
- 367 Hunter, William et al. (2017). *ToPy - Topology Optimization with Python*. GitHub. URL: <https://github.com/williamhunter/topy>.

- 393 Le Quilliec, Guenael (2014). "Topology Optimization Procedure TOPOP-
394 TIM and Other Various Developments Made with Cast3M". In: DOI:
395 10 . 13140 / 2 . 1 . 2718 . 3682. URL: <http://rgdoi.net//10.13140/2.1.2718.3682> (visited on 02/29/2024).
- 396
- 397 McTigue, D. F. (Nov. 10, 1987). "Elastic Stress and Deformation near a Fi-
398 nite Spherical Magma Body: Resolution of the Point Source Paradox".
399 In: *Journal of Geophysical Research: Solid Earth* 92.B12, pp. 12931–
400 12940. ISSN: 0148-0227. DOI: 10.1029/JB092iB12p12931. URL: <https://agupubs.onlinelibrary.wiley.com/doi/10.1029/JB092iB12p12931>
401 (visited on 02/27/2024).
- 402
- 403 Mogi, Kiyo (1958). "Relations between the Eruptions of Various Volcanoes
404 and the Deformations of the Ground Surfaces around Them". In: *Earthq
405 Res Inst* 36, pp. 99–134.
- 406 Parks, Michelle et al. (Jan. 23, 2024). "Data and Geodetic Modelling Results
407 for Science Article "Fracturing and Tectonic Stress Drives Ultra-Rapid
408 Magma Flow into Dikes"". In: URL: <https://osf.io/9rcq7/> (visited on
409 08/21/2024).
- 410 Sigmund, O. (Apr. 1, 2001). "A 99 Line Topology Optimization Code Writ-
411 ten in Matlab". In: *Structural and Multidisciplinary Optimization* 21.2,
412 pp. 120–127. ISSN: 1615-1488. DOI: 10.1007/s001580050176. URL: <https://doi.org/10.1007/s001580050176> (visited on 08/22/2024).
- 413
- 414 Sigmund, Ole and Kurt Maute (Dec. 1, 2013). "Topology Optimization Ap-
415 proaches". In: *Structural and Multidisciplinary Optimization* 48.6, pp. 1031–
416 1055. ISSN: 1615-1488. DOI: 10.1007/s00158-013-0978-6. URL: <https://doi.org/10.1007/s00158-013-0978-6> (visited on 08/21/2024).
- 417
- 418 Sigmundsson, Freysteinn et al. (Mar. 15, 2024). "Fracturing and Tectonic
419 Stress Drive Ultrarapid Magma Flow into Dikes". In: *Science* 383.6688,
420 pp. 1228–1235. DOI: 10.1126/science.adn2838. URL: <https://www.science.org/doi/10.1126/science.adn2838> (visited on 08/21/2024).
- 421
- 422 Slavov, Stoyan and Mariya Konsulova-Bakalova (Jan. 15, 2019). "Optimizing
423 Weight of Housing Elements of Two-stage Reducer by Using the Topology
424 Management Optimization Capabilities Integrated in SOLIDWORKS: A
425 Case Study". In: *Machines* 7.1, p. 9. ISSN: 2075-1702. DOI: 10.3390/
426 machines7010009. URL: <https://www.mdpi.com/2075-1702/7/1/9>
427 (visited on 08/22/2024).
- 428
- 429 Taylor, Nicola C., Jessica H. Johnson, and Richard A. Herd (Nov. 1, 2021).
430 "Making the Most of the Mogi Model: Size Matters". In: *Journal of
431 Volcanology and Geothermal Research* 419, p. 107380. ISSN: 0377-0273.
432 DOI: 10 . 1016 / j . jvolgeores . 2021 . 107380. URL: <https://www.sciencedirect.com/science/article/pii/S0377027321002092> (vis-
433 ited on 08/22/2024).

- 434 Trasatti, Elisa (July 1, 2022). "Volcanic and Seismic Source Modeling: An
435 Open Tool for Geodetic Data Modeling". In: *Frontiers in Earth Science*
436 10. ISSN: 2296-6463. DOI: 10.3389/feart.2022.917222. URL: <https://www.frontiersin.org/journals/earth-science/articles/10.3389/feart.2022.917222/full> (visited on 08/21/2024).
- 437 Velez, Maria Laura et al. (Apr. 30, 2011). "Deformation of Copahue Vol-
438 cano: Inversion of InSAR Data Using a Genetic Algorithm". In: *Journal*
439 of *Volcanology and Geothermal Research* 202.1, pp. 117–126. ISSN: 0377-
440 0273. DOI: 10.1016/j.jvolgeores.2011.01.012. URL: <https://www.sciencedirect.com/science/article/pii/S0377027311000394>
441 (visited on 08/22/2024).
- 442 Yang, Xue-Min, Paul M. Davis, and James H. Dieterich (1988). "Deforma-
443 tion from Inflation of a Dipping Finite Prolate Spheroid in an Elastic
444 Half-Space as a Model for Volcanic Stressing". In: *Journal of Geophys-
445 ical Research: Solid Earth* 93.B5, pp. 4249–4257. ISSN: 2156-2202. DOI:
446 10.1029/JB093iB05p04249. URL: <https://onlinelibrary.wiley.com/doi/abs/10.1029/JB093iB05p04249> (visited on 08/22/2024).

Conclusion

In this study, we have presented a code for solving inverse problems in volcano geodesy by combining the Finite Element Method (FEM) with global parametric optimization techniques and used it to assess the origin the 2011-2015 inflation at Eyjafjallajökull. Then, we developed a new approach to solve inverse problem on magmatic chamber based on shape optimization, a technique taken from the engineering field.

Both methods showed promising but not definitive results. The shape optimisation being a brand new method in this context, it strongly needs more tests to better understand its behavior in order to reach result that could be confidently used in operational cases for magma chamber inversion.

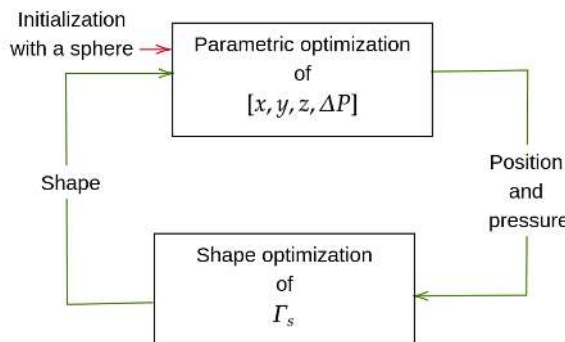


Figure C1: Overall loop optimizing first a spherical source as a rigid body by changing its internal pressure and location, and then optimizing the shape of the source by deforming it. Once a new shape is found the parametric optimization moves it and change the pressure again. The loop stops when an overall convergence is found: no significant modification are done to the shape and the parameters.

To overcome limits of both method we described in their respective chapter, an overall optimisation procedure could be envisaged, as explained on figure C1. In this regard, both shape and controlling parameters would be optimized, providing an high level of confidence in the result. We could even parametrically optimize additional constraints such as the volume of the source to ensure better convergence of the shape optimization. Of course, this procedure would come at a high computational cost, and so it should run on high performance cluster rather than on personal computers as it is the case now. We

could also imagine a way to modify the architecture to let this loop run in parallel to speed up the overall computation time.

Models we presented herein are purely elastic. This involves modelling ground change as instantaneous without any time dependence. It is sufficient to capture overall trends like inflation and deflation of magmatic source and roughly assess the current state of the reservoirs, but may lack of details. For instance, it is known that warmer part of the crust behave viscoelastically, including parts that are deeper (because of geothermal gradient) and part that are closer from magmatic sources. This may cause relaxation phenomena influencing ground motion even after magmatic activity and thus bias the results of an elastic model, as studied by Del Negro, Currenti, and Scandura [2009](#). We can also cite other phenomena such as complex magma rheology or poroelasticity (Paul Segall [2019](#), Alshembari et al. [2022](#)) that can be of strong influence on the overall behaviour. Fortunately enough, such phenomena can be taken into account by forward numerical models at a higher computational cost. Hence, they could be included in the optimization loop for richer and more accurate inversions result.

A last phenomenon acting mainly on Icelandic volcanoes to mention is the effect of glacier loading and unloading on the magmatic activity. It is suspected that rapid retreat of glacier due to climate change may change stress condition of the magma reservoir and trigger unexpected magmatic activity. At a larger scale, the [glacial isostatic adjustment](#) signal is also affected and may cause inaccurate estimate of the change in the Up components due to magmatic activity. Such complexity should be incorporated in future modelling and are currently under examination of the ISVOLC research project funded by the national research agency of Iceland (Parks and ISVOLC Team [2024](#)).

The results presented here serve as a proof-of-concept for the application of FEM-based inversion methods in geophysics. Future work will focus on further developing and refining this approach to address the limitations identified herein. Ultimately, we hope that this study will contribute to a greater understanding of the complex processes that shape our planet and provide insights into the subsurface structures that underlie them.



Figure C2: Rams climbing old basaltic formations in Kópasker, North-East Iceland. This picture show the crucial importance of volcanic activity assessment in Iceland, where any aspect of life including breeding may be affected by renewed activity. A massive seism hit Kópasker in 1976, causing major destructions in the farms.

Appendices

A Overview of Iceland geology

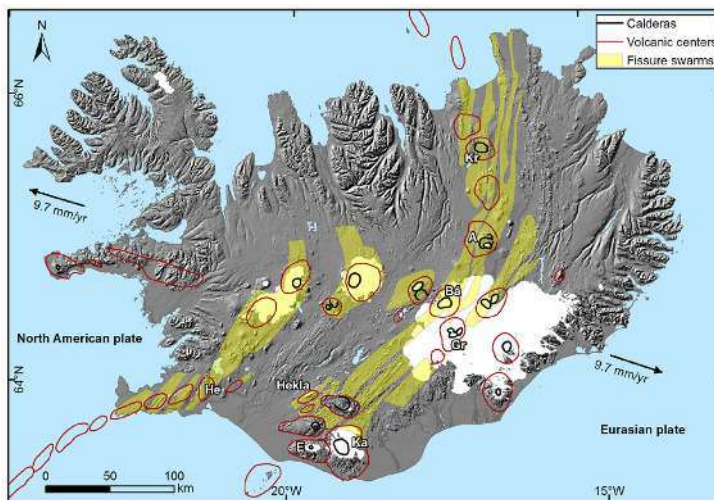


Figure A1: Map of volcanic systems of Iceland (outlined in red). Note Eyjafjallajokull on the South marked with the acronym E. The overall direction of the plate spreading is also marked with the black arrows. The volcanic systems are following the ridge outside of the immersed part. Extracted from Freysteinn Sigmundsson, Parks, Pedersen, et al. 2018.

Iceland is located on the Middle Atlantic Ridge (MAR), which is the boundary between the Eurasian and North American plates. These two plates are diverging at a rate of 17 mm yr^{-1} (Drouin and Freysteinn Sigmundsson 2019), and this divergent motion causes magma generation that forms the ridge. In addition to this mechanism, Iceland is located on a hot spot that causes extensive magmatic activity. This hotspot is thought to be the surface consequence of a mantle plume, a rising part of the mantle containing abnormally hot material compared to the surrounding area. Over time, this led to the formation of an island, Iceland. The oldest rocks found in Iceland are about 15 million years old. In comparison, the opening of the North Atlantic Ocean, which formed the current ridge and seafloor, took place 60 million years ago. In short, the oldest rocks are found in the west and east of Iceland, while the youngest are within the active volcanic zones. Because of the divergent motion, new material is created at the hotspot during a volcanic event in

place of the old material that is pushed away (Freysteinn Sigmundsson 2006).

The volcanic areas mostly follow the path of the MAR, with some exceptions, as shown in the figure A1. 32 active volcanic systems have been identified, with frequent eruptions. Iceland is mostly covered with basalt resulting from this activity.

In addition to this peculiar geological setting, the latitude at which Iceland lies is responsible for its cold climate and the presence of glaciers covering about 10 % of its surface. Therefore, many volcanic systems such as Eyjafjallajökull, Katla, Badabunga and others are subglacial. Subglacial volcanism can cause massive floods called jökullhlaups as well as explosive activity. Table mountains and horizontal structures found in Iceland are characteristic of subglacial volcanism.

Due to global warming since the 19th century, the general trend is the retreat of these glaciers, which is accelerating with time (adalgeirsdottir2020). This leads to a rapid unloading of the earth's crust, causing the so-called [glacial isostatic adjustment](#). Due to the viscosity of the mantle, the crust reacts to this unloading with a visco-elastic delay, causing a general upwelling of the Icelandic surface, peaking at a rate of 34 mm yr⁻¹ for the Up component in some areas (Drouin and Freysteinn Sigmundsson 2019).

B Global Navigation Satellite System (GNSS)

The first and most intuitive method used to describe long timescale movements of the ground (as opposed to fast ones lasting a couple of seconds or minutes) consists in measuring the position of a fixed point on the ground at regular intervals, in order to track the changes in position. Nowadays, this is achieved by using GNSS positioning. A Global Navigation Satellite System (GNSS) is a system composed of a constellation of satellites orbiting around the Earth and broadcasting electromagnetic signals. Several kinds of GNSS systems exist, such as the American GPS, the European GALILEO or the Russian GLONASS.



Figure A2: Campaign GNSS station *FAUS* (the names of the stations are usually composed of 4 letters). The antenna (in white) is mounted on a tripod (in yellow) precisely positioned over a benchmark (not visible). The black box on the left contains the receiver supplied by the battery behind it. This picture was taken during the field trip.

Roughly speaking, by receiving these signals from at least 4 satellites a receiver can compute its relative distance to each of them by measuring the time at which the signals travel. With the ephemerides (satellites trajectories), the final position of the receiver in a reference frame is known. Depending on the number of observations made by the receiver and the acquisition time, the uncertainty regarding the position of the point varies. For civil application such as positioning in smartphone, the acquisition timescale is about one second and the precision reaches tens of meters, while for geodetic measurement instruments, the acquisition time ranges from 8 hours to 24 hours and a millimeter scale precision is achieved Dzurisin 2007. This is of course a rough overview of the principle and the GNSS positioning, which is a complex area of research.

In practice, the idea is to precisely position a GNSS antenna relatively to a benchmark fixed on the ground (usually a metal dot embedded in concrete), which is the measured point. This antenna is connected to a receiver computing the raw observation data and to a power supply (see figure A2).

The GNSS measurements can be done all year round at continuous stations where a power supply is provided (for instance by solar panels). They can be used to track changes

in position over days in sites of interest. There are also campaign sites where the position of the benchmark is measured during field campaigns, usually taking place once a year, by setting up a temporary GNSS station supplied by batteries for a couple of days. This allows to track long-term movements – unfolding during a year at least – at remote sites.

Around Eyjafjallajökull, both kind of GPS sites are present (Fig. 1.1), and one of the first tasks of this internship has been to carry out new measurements on campaign sites. This has involved two days of field trip around the volcano to set up 10 temporary instruments and retrieving them after 3 days of measurements. The field trip was led by the technician Sveinbjörn Steinþórsson, and Fjóla Sigurðardóttir, a student working on the same data, was here to help as well.

Existing and collected raw data for continuous and campaign sites near the volcano has been processed using the command line tool GAMIT-GLOBK Floyd 2024 on the *Strokkur* computing facility of the institute with the help of Chiara Lanzi (PhD student in Geophysics). This software computes the precise 3-dimensional position of each site over time in a standard reference frame from the data, performing complex ambiguity and atmospheric noise reduction algorithm. At the end of the process, we have access to the 3D position time series expressed in East, North and Up components for each station.

C Interferometric Synthetic Aperture Radar (InSAR)

While continuous GNSS stations are useful to achieve a good temporal resolution in ground displacement, InSAR (Interferometric analysis of Synthetic Aperture Radar satellite images) is a complementary tool widely used in geodetic measurements. It provides displacement measurements over large areas with very good spatial resolution.

The SAR acquisition is an active process : the satellite antenna sends an electromagnetic pulse perpendicularly to the flight direction with a certain incidence angle, and captures the signal reflected by the ground. This result in an image in which the pixels are bearing two quantities : the phase and the amplitude of the returned wave. The amplitude mainly depends on the terrain reflecting the wave and its geometry, while the phase varies with the distance travelled by the wave.

Interferometry occurs if a second picture is taken from the same position after a certain amount of time. Indeed, SAR satellites follow near polar orbits, meaning that their trajectory intersects the poles, enabling them to periodically fly over the same spot (see scheme figure A3). The phase difference pixel per pixel of the two images is computed, creating an interferogram. This phase difference is hence a measure of the ground displacement between the two acquisition times, and has a precision of the same order of magnitude than the wavelength, which is around 28 mm for the COSMO-SkyMed Italian satellite, one of the chosen data source of this study (Dzurisin 2007).

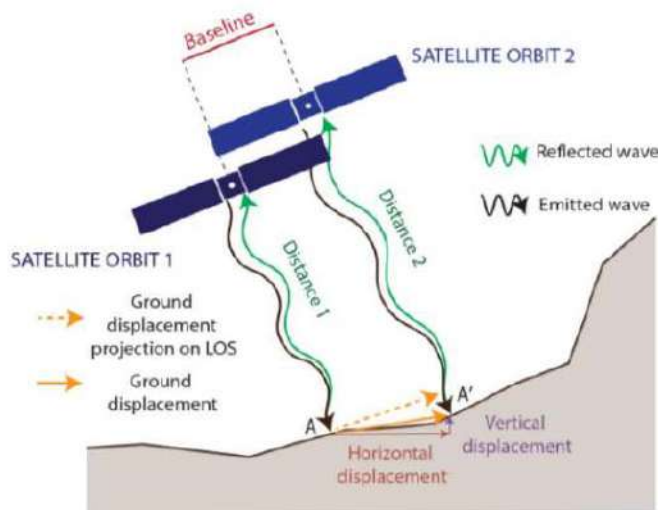


Figure A3: Diagram showing InSAR principle, extracted from the report of Grémion 2020. The baseline is the distance between two successive positions of the satellite.

The displacement values are scalar because the InSAR process is sensitive to displacement only in one direction: changes are measured if there is a displacement towards the satellite or away from it. Thus, what is measured is the projection of the ground displacement vector on the Line Of Sight vector (LOS) pointing in the look direction of the satellite (fig. A3). One displacement map formed by InSAR is insufficient to have a complete idea of the displacement within an area, that is why InSAR data sets are often completed by interferograms taken from different perspectives with different LOS direction. To reduce uncertainties, there is at least one descending (satellite flying towards South) and one ascending (satellite flying towards North) interferograms in order to reproject the LOS displacement in terms of Up, and East components.

D Geodetic analytical models

The simplest and most straightforward models of a magma chamber are analytical. In order to obtain an analytical expression for the surface displacements, strong assumptions are made : the Earth is described as a flat, homogeneous, isotropic and elastic half-space. The pressure source is a surface of simple shape with a uniform pressure load at the boundary. The simplest of these is the Mogi 1958 model, which assumes that the pressure source is a point (this assumption holds if the radius of the source is small relatively to the depth). An equation can be derived and the displacement field (u_r, u_z) expressed on the surface in cylindrical coordinates can be expressed as follows :

$$u_z = \frac{(1 - \nu)\Delta P\alpha^3}{G} \frac{d}{(r^2 + d^2)^{1.5}} \quad (2.1)$$

$$u_r = \frac{(1 - \nu)\Delta P\alpha^3}{G} \frac{r}{(r^2 + d^2)^{1.5}} \quad (2.2)$$

where G , ν are the shear and Poisson's moduli of the rocks, α is the radius of the source, (d, r) are the classical cylindrical coordinates (vertical and radial distance from the source). More advanced models consider more realistic shapes for a magma reservoir, such as a finite volume sphere (McTigue 1987), a dike (vertical plane feature) or a sill (horizontal plane feature) Okada 1985. These models explicitly include the source parameters (α , ΔP and source localization for a Mogi model) in their expression. The more complex the model is, the more parameters are needed to describe the source.

Taking advantage of the low computational cost and parametric nature of these models, they are widely used in inversion schemes to find the most likely source parameters. The observed surface displacements are the inputs, and inversion algorithms return the optimal source parameters by minimizing a cost function representative of the error between these observations and the displacements predicted by the model (given by its analytical expression). Inversion software is numerous and implements different inversion schemes. For example, GBIS (Geodetic Bayesian Inversion Software) uses Bayesian inversions and is widely employed at the Institute (Bagnardi and Andrew Hooper 2018).

Despite their strong assumptions, these models can reproduce complex displacement patterns by combining several sources, as shown in a very recent article (Freysteinn Sigmundsson, Parks, Geirsson, et al. 2024) analysing the November 2023 dike intrusion (i.e. the magma ascent in the shallow crust after magma chamber breakthrough) in the Reykjanes peninsula. Both the sill-shaped magma chamber and the dike are modelled with great precision.

E Pipeline benchmarking

To ensure the correct functioning of the pipeline we built, it was benchmarked with simple cases. This is a common practice to benchmark FEM models for known solutions, useful to assess their relevance. Here we chose to model a finite spherical pressure source embedded in an elastic half-space. The analytical solution for the surface displacement field exists and has been derived [McTigue 1987](#).

The parameters for the analytical and numerical models are as follows:

- Elastic moduli : $E = 30GPa$ (Young modulus), $\nu = 0.25$ (Poisson's ratio)
- Source location : $x = 0km$ (East), $y = 0km$ (North), $z = -5km$
- Source geometry : sphere of radius $\alpha = 500m$
- Pressure change : $\Delta P = 45MPa$

For the FEM model, a domain of $60 \times 60 \times 40km$ is modelled, with a free boundary condition on the top surface, a rolling condition (tangential displacements allowed) on the sides, an embedding on the bottom surface and a uniform loading on the source surface (as showed fig. 1.5).

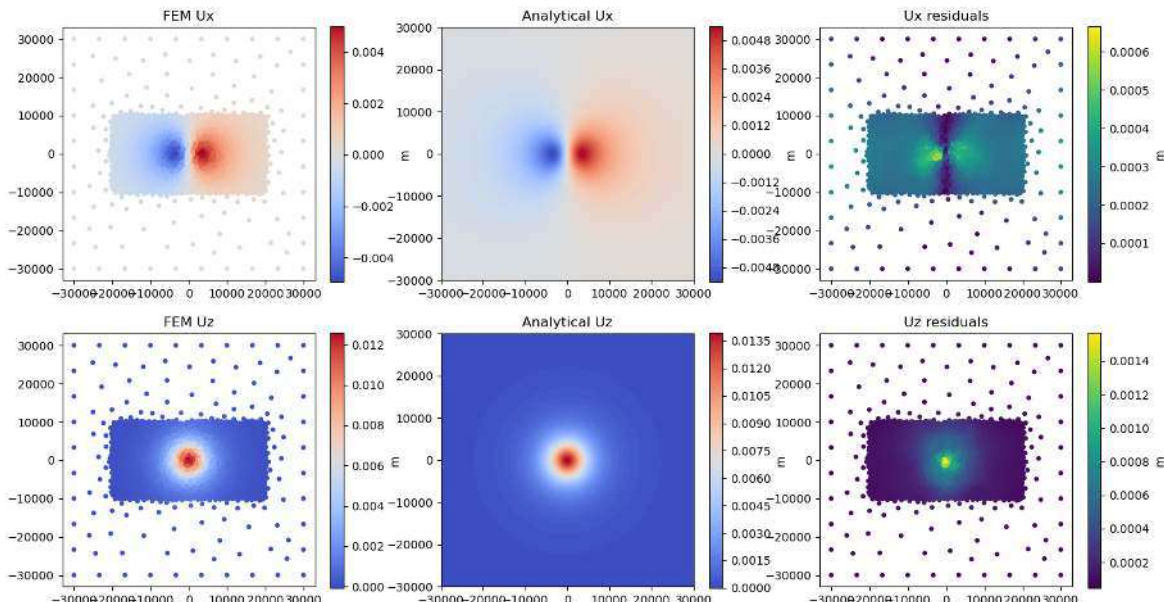


Figure A4: Vertical and horizontal displacement field for the uniform mesh benchmarking. RMS values are $\Delta U_x = 1.2e-4m$, $\Delta U_y = 2.1e-4m$, $\Delta U_z = 3.3e-4m$

With a simple fine uniform mesh (see figure A4) the results are satisfying, as shown in A4. The misfit is evaluated with the RMS of the displacement calculated at the integration points of the FEM model and the analytical displacement at the same points. The error given by the RMS values is in accordance with the error made by the same kind of FEM models O'Hara [2023](#) ($\Delta U_x = 2.0e-4m$, $\Delta U_y = 2.8e-5m$, $\Delta U_z = 9.0e-4m$ in the mentioned work).

F Additional figures

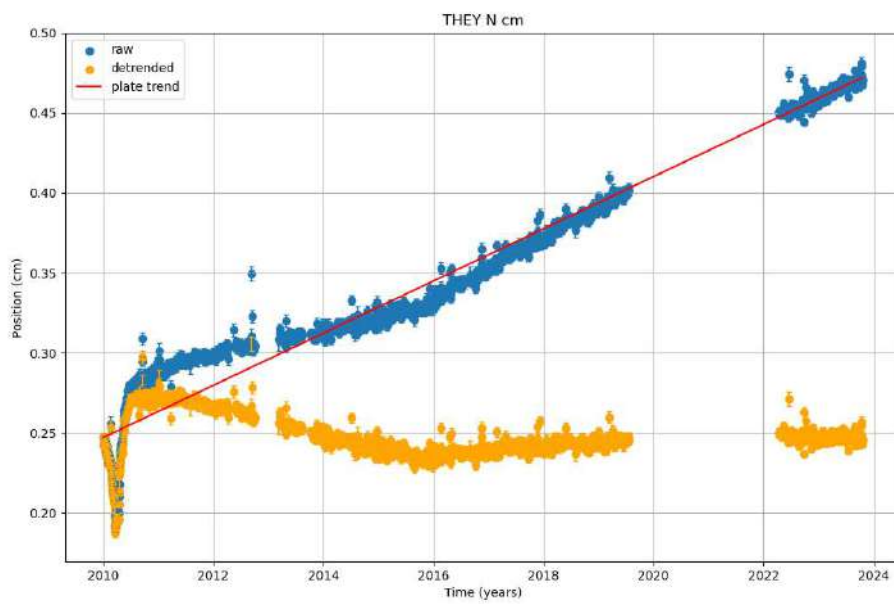


Figure A5: Time series of the North displacement of *THEY* before and after removing the speed of the Eurasian plate using the ITRF2014 model.

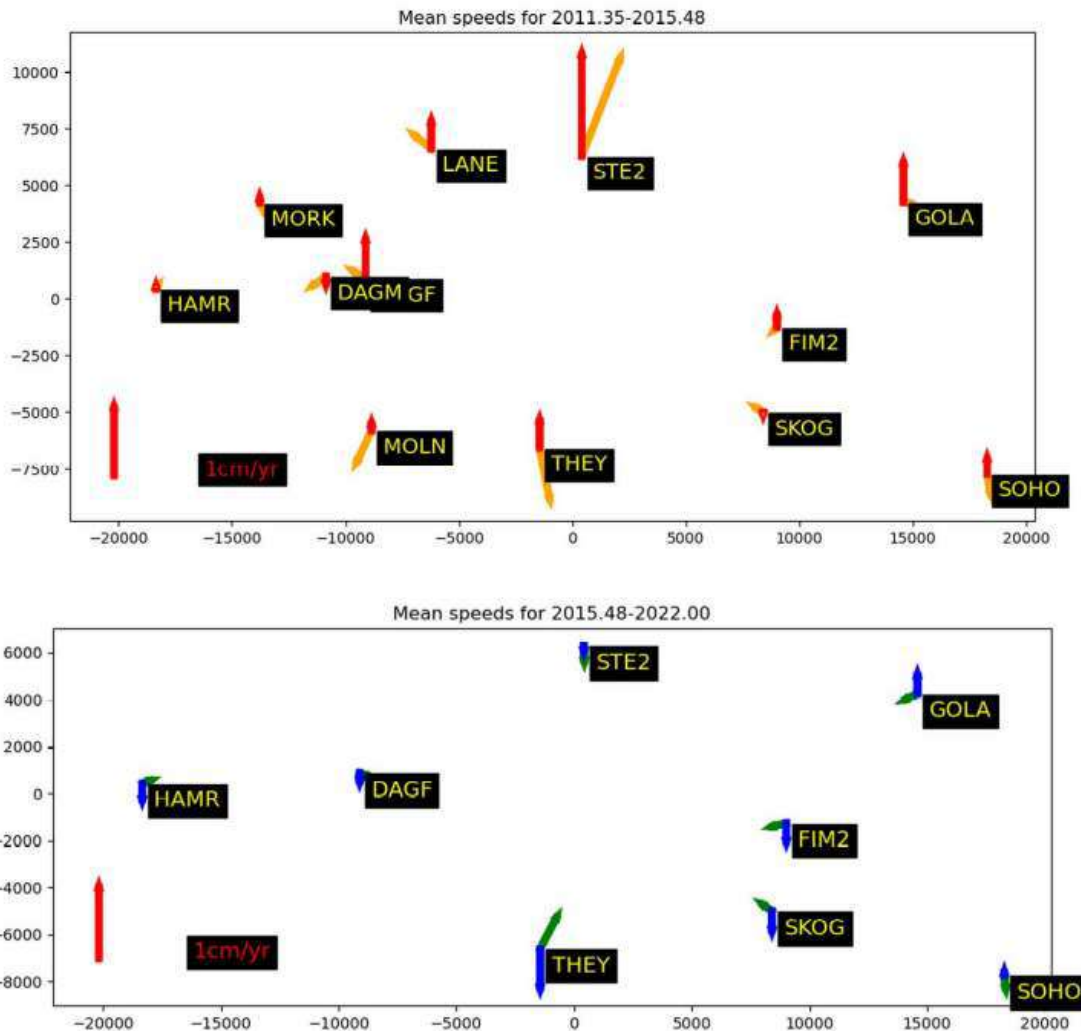


Figure A6: Map of the 3D GNSS displacements rates for the 2011-2015 *TP2* period (top) and the 2015-2022 *TP3* (bottom) period. The vertical arrows show the Up components, the others show the horizontal (East and North) components. It is clear that during *TP3*, we observe a deflation pattern: the stations around the volcano are converging. However, the phenomenon is clearly slower compared to the inflation rates above.

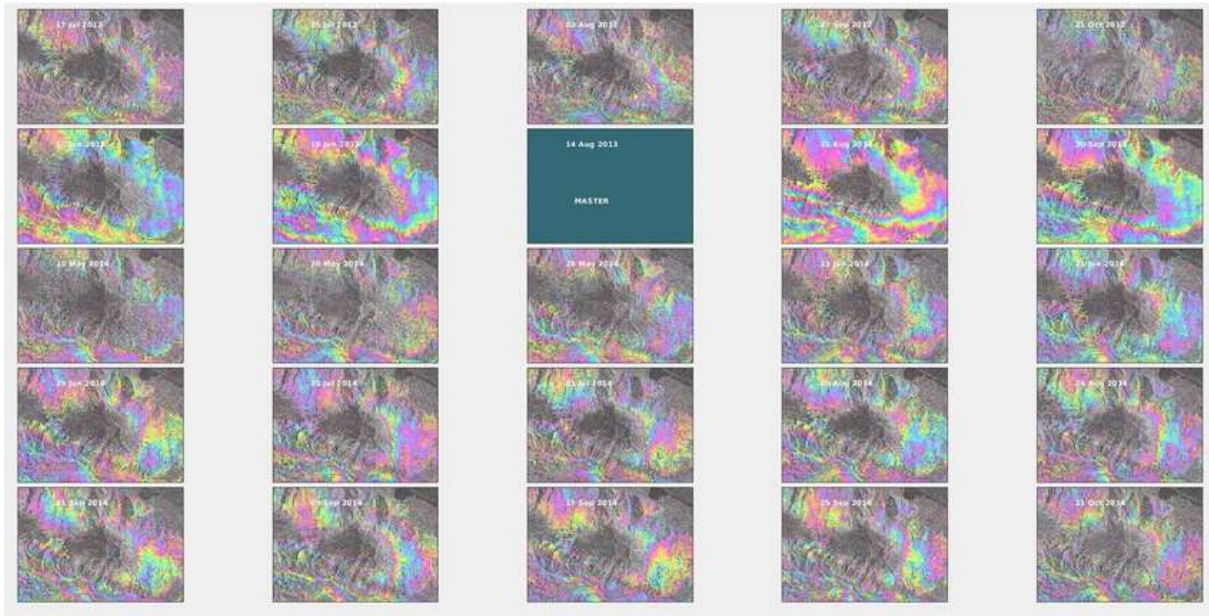


Figure A7: All wrapped CSK A32 interferograms used in the processing. The color patterns are called fringes, and one complete colour cycle correspond to a 2π phase shift so a change in LOS displacement of the wavelength (28 mm). The process of shifting from fringes representation to simple LOS displacement is called unwrapping. Note on some interferograms strong and large signals, corresponding to atmospheric perturbations.

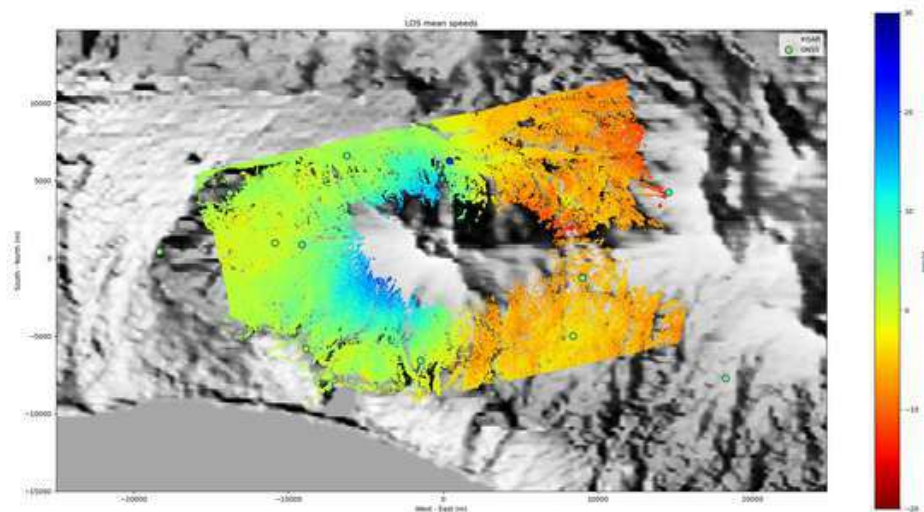


Figure A8: First InSAR map of Eyjafjallajökull. The circled dots are the GNSS data, clearly diverging for the background InSAR data. The East-West divergent pattern may indicate a small **dike** intrusion which was out of the scope of the modelling.

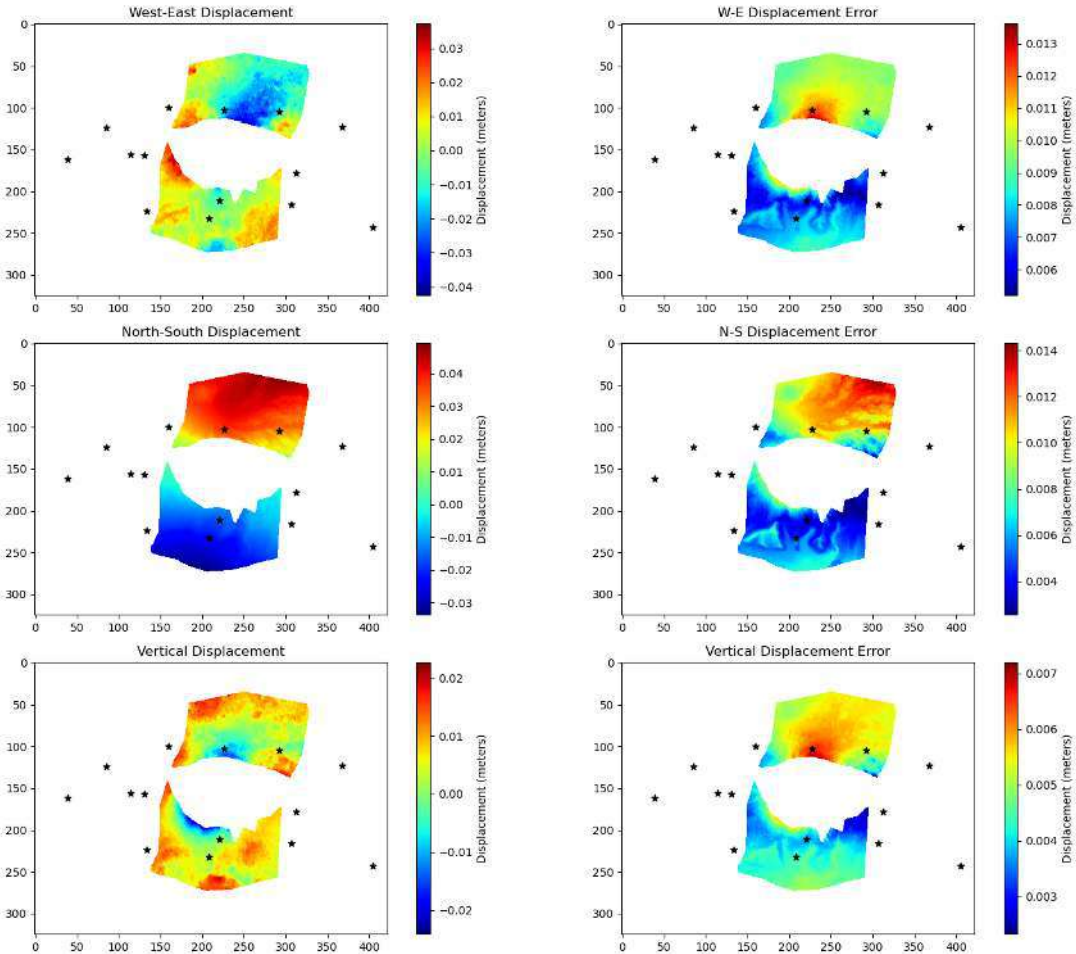


Figure A9: Attempt to form a 3D displacement map of the inflation. After reprojecting and interpolating the data (GNSS points and T125, T132 InSAR tracks) with QGIS, we use the SISTEM tool developed by Guglielmino et al. 2011. It would have been used as unique data source for inversion, setting aside the problem of arbitrary weighting the datasets. The overall inflation trend was well depicted by the output, however it was useless: strong artefacts are remaining in the signal with no physical explanation and the residuals are of the same order of magnitude as the data.

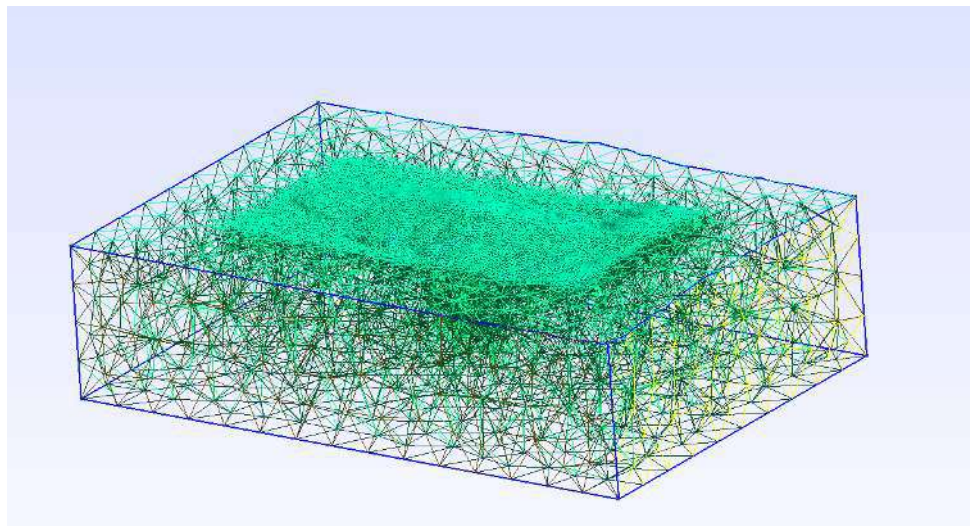


Figure A10: Close-up view of a portion of the mesh containing the topography of the volcano.

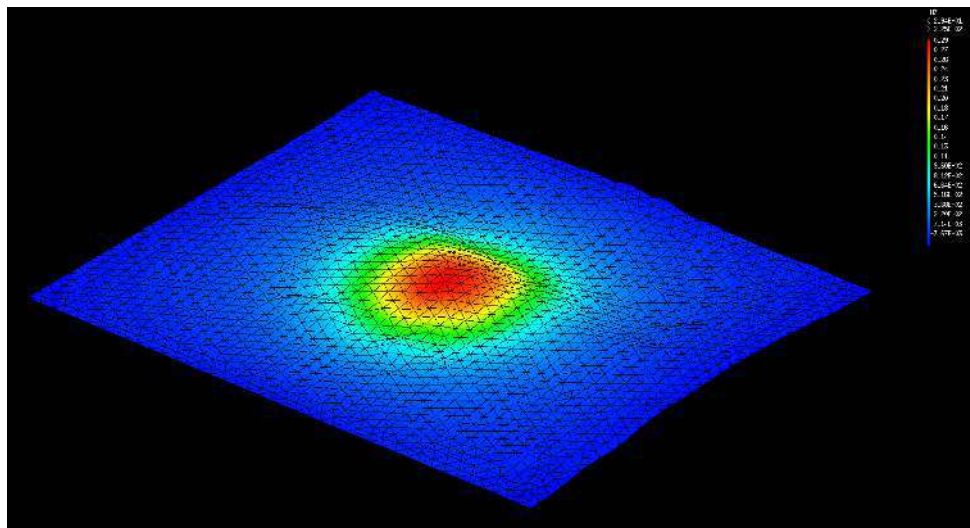


Figure A11: Surface mesh coloured with the vertical displacement intensity after solving of a forward model by Cast3m

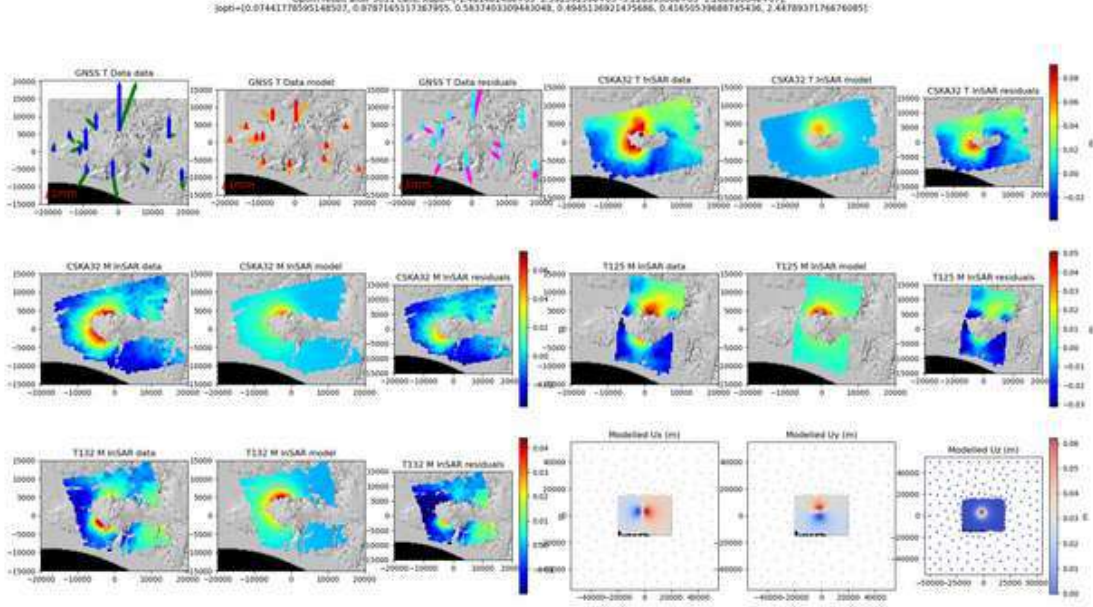


Figure A12: Best result found after 5000 evaluations of J . Here, the CSK A32 dataset is shown twice only to compare different processing approach on the interferograms. The best parameter vector found is $p_{opt} = (-1.48\text{km}, 32.60\text{km}, -3.23\text{km}, 12.7\text{MPa})$ for a $R = 800\text{m}$. This is not consistent with the BOBYQA result, likely because the meshing parameters were modified for this test.

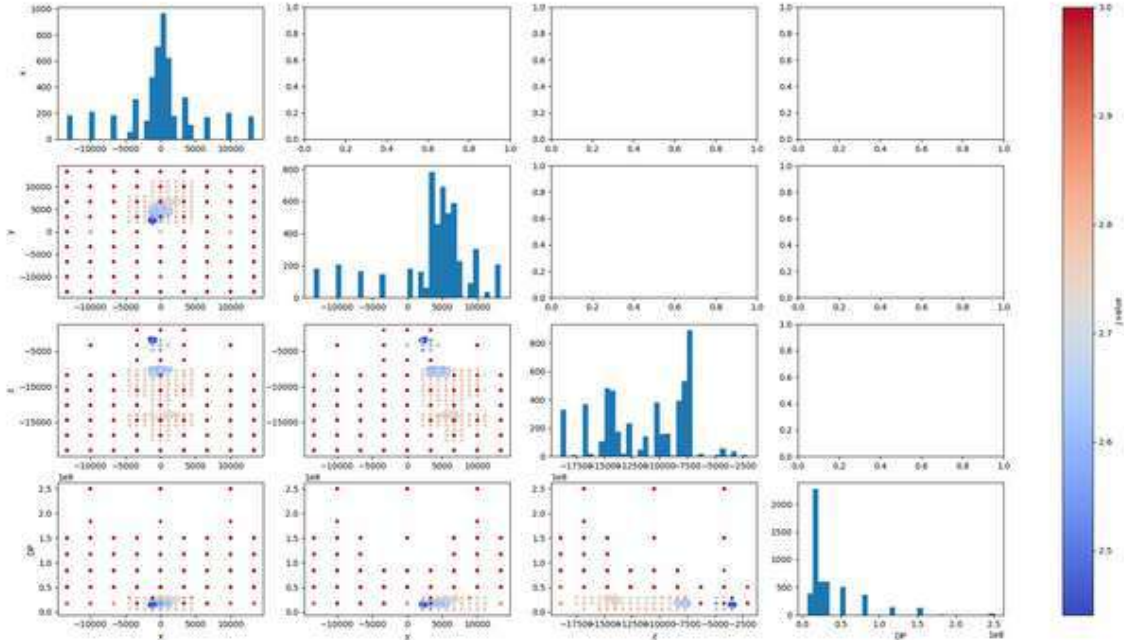


Figure A13: Distribution of the evaluation point within the search space, with the DIRECT algorithm here. The regularity of the evaluation is due to the DIRECT strategy which cuts the hyperspace in regular hyper-rectangles. The distribution are well compacted in the search space for each parameter showing the evaluation domain was adequately chosen.

References

- Albino, F. and F. Sigmundsson (2014). "Stress Transfer between Magma Bodies: Influence of Intrusions Prior to 2010 Eruptions at Eyjafjallajökull Volcano, Iceland". In: *Journal of Geophysical Research: Solid Earth* 119.4, pp. 2964–2975. ISSN: 2169-9356. DOI: [10.1002/2013JB010510](https://doi.org/10.1002/2013JB010510). URL: <https://onlinelibrary.wiley.com/doi/abs/10.1002/2013JB010510> (visited on 08/30/2024).
- Alshembari, Rami et al. (2022). "Poroelastic Mechanical Behavior of Crystal Mush Reservoirs: Insights Into the Spatio-Temporal Evolution of Volcano Surface Deformation". In: *Journal of Geophysical Research: Solid Earth* 127.10, e2022JB024332. ISSN: 2169-9356. DOI: [10.1029/2022JB024332](https://doi.org/10.1029/2022JB024332). URL: <https://onlinelibrary.wiley.com/doi/abs/10.1029/2022JB024332> (visited on 08/30/2024).
- Altamimi, Zuheir et al. (Aug. 2016). "ITRF2014: A New Release of the International Terrestrial Reference Frame Modeling Nonlinear Station Motions". In: *Journal of Geophysical Research: Solid Earth* 121.8, pp. 6109–6131. ISSN: 2169-9313, 2169-9356. DOI: [10.1002/2016JB013098](https://doi.org/10.1002/2016JB013098). URL: <https://agupubs.onlinelibrary.wiley.com/doi/10.1002/2016JB013098> (visited on 02/28/2024).
- Bagnardi, Marco and Andrew Hooper (July 2018). "Inversion of Surface Deformation Data for Rapid Estimates of Source Parameters and Uncertainties: A Bayesian Approach". In: *Geochemistry, Geophysics, Geosystems* 19.7, pp. 2194–2211. ISSN: 1525-2027, 1525-2027. DOI: [10.1029/2018GC007585](https://doi.org/10.1029/2018GC007585). URL: <https://agupubs.onlinelibrary.wiley.com/doi/10.1029/2018GC007585> (visited on 02/29/2024).
- Belart, Joaquín M. C. et al. (June 2019). "The Geodetic Mass Balance of Eyjafjallajökull Ice Cap for 1945–2014: Processing Guidelines and Relation to Climate". In: *Journal of Glaciology* 65.251, pp. 395–409. ISSN: 0022-1430, 1727-5652. DOI: [10.1017/jog.2019.16](https://doi.org/10.1017/jog.2019.16). URL: https://www.cambridge.org/core/product/identifier/S0022143019000169/type/journal_article (visited on 02/27/2024).
- Cartis, Coralia, Lindon Roberts, and Oliver Sheridan-Methven (Aug. 3, 2022). "Escaping Local Minima with Local Derivative-Free Methods: A Numerical Investigation". In: *Optimization* 71.8, pp. 2343–2373. ISSN: 0233-1934, 1029-4945. DOI: [10.1080/02331934.2021.1883015](https://doi.org/10.1080/02331934.2021.1883015). URL: <https://www.tandfonline.com/doi/full/10.1080/02331934.2021.1883015> (visited on 08/29/2024).
- Dapogny, Charles and Florian Feppon (Oct. 31, 2023). "Shape Optimization Using a Level Set Based Mesh Evolution Method: An Overview and Tutorial". In: *Comptes Rendus. Mathématique* 361.G8, pp. 1267–1332. ISSN: 1778-3569. DOI: [10.5802/crmath.498](https://doi.org/10.5802/crmath.498).

- URL: <https://comptes-rendus.academie-sciences.fr/mathematique/articles/10.5802/crmath.498/> (visited on 08/02/2024).
- Del Negro, Ciro, Gilda Currenti, and Danila Scandura (Feb. 1, 2009). "Temperature-Dependent Viscoelastic Modeling of Ground Deformation: Application to Etna Volcano during the 1993–1997 Inflation Period". In: *Physics of the Earth and Planetary Interiors* 172.3, pp. 299–309. ISSN: 0031-9201. DOI: [10.1016/j.pepi.2008.10.019](https://doi.org/10.1016/j.pepi.2008.10.019). URL: <https://www.sciencedirect.com/science/article/pii/S0031920108003087> (visited on 08/30/2024).
- Drouin, Vincent and Freysteinn Sigmundsson (July 28, 2019). "Countrywide Observations of Plate Spreading and Glacial Isostatic Adjustment in Iceland Inferred by Sentinel-1 Radar Interferometry, 2015–2018". In: *Geophysical Research Letters* 46.14, pp. 8046–8055. ISSN: 0094-8276, 1944-8007. DOI: [10.1029/2019GL082629](https://doi.org/10.1029/2019GL082629). URL: <https://agupubs.onlinelibrary.wiley.com/doi/10.1029/2019GL082629> (visited on 02/27/2024).
- Dzurisin, Daniel (2007). *Volcano Deformation: Geodetic Monitoring Techniques*. Springer-Praxis Books in Geophysical Sciences. Berlin ; New York : Chichester, UK: Springer ; Praxis. 441 pp. ISBN: 978-3-540-42642-4.
- Fialko, Yuri, Yakov Khazan, and Mark Simons (July 1, 2001). "Deformation Due to a Pressurized Horizontal Circular Crack in an Elastic Half-Space, with Applications to Volcano Geodesy". In: *Geophysical Journal International* 146.1, pp. 181–190. ISSN: 0956-540X. DOI: [10.1046/j.1365-246X.2001.00452.x](https://doi.org/10.1046/j.1365-246X.2001.00452.x). URL: <https://doi.org/10.1046/j.1365-246X.2001.00452.x> (visited on 09/02/2024).
- Fletcher, Karen (2007). *InSAR Principles: Guidelines for SAR Interferometry Processing and Interpretation*. ESA TM 19. Noordwijk, the Netherlands: ESA Publications Division, ESTEC. ISBN: 978-92-9092-233-9.
- Floyd, M. (2024). *GAMIT/GLOBK Documentation*. GAMIT/GLOBK Documentation. URL: <http://geoweb.mit.edu/gg/docs.php> (visited on 02/27/2024).
- Geuzaine, Christophe (n.d.). *Gmsh Manual 4.13.1*. URL: <https://gmsh.info/doc/texinfo/gmsh.html>.
- Geuzaine, Christophe, Jean-Francois Remacle, and P Dular (2009). "Gmsh: A Three-Dimensional Finite Element Mesh Generator". In: *International Journal for Numerical Methods in Engineering* 79.11, pp. 1309–1331.
- Greiner, Sonja HM (2021). "Including Topography and a 3D-elastic Structure into a Finite-Element Deformation Model of Grímsvötn, Iceland". PhD thesis. URL: <http://hdl.handle.net/1946/38435>.
- Grémion, Shan (2020). "Eyjafjallajökull Ground Deformation History between 2009 and 2019 Using InSAR Timeseries and Magma Sources Modelling". MA thesis. University of Iceland.
- Guðmundsson, Magnús T. and Ármann Höskuldsson (2019). *Icelandic Volcanoes*. URL: <https://icelandicvolcanos.is/?volcano=EYJ> (visited on 02/26/2024).
- Guglielmino, Francesco et al. (June 2011). "Simultaneous and Integrated Strain Tensor Estimation From Geodetic and Satellite Deformation Measurements to Obtain Three-Dimensional Displacement Maps". In: *IEEE Transactions on Geoscience and Remote Sensing* 49.6, pp. 1815–1826. ISSN: 0196-2892, 1558-0644. DOI: [10.1109/TGRS.2010.2103078](https://doi.org/10.1109/TGRS.2010.2103078). URL: <http://ieeexplore.ieee.org/document/5710978/> (visited on 09/01/2024).
- Hecht, F. (2012). "New Development in FreeFem++". In: *Journal of Numerical Mathematics* 20.3-4, pp. 251–265. ISSN: 1570-2820. URL: <https://freefem.org/>.

- Hickey, James and Joachim Gottsmann (June 2014). "Benchmarking and Developing Numerical Finite Element Models of Volcanic Deformation". In: *Journal of Volcanology and Geothermal Research* 280, pp. 126–130. ISSN: 03770273. DOI: [10.1016/j.jvolgeores.2014.05.011](https://doi.org/10.1016/j.jvolgeores.2014.05.011). URL: <https://linkinghub.elsevier.com/retrieve/pii/S037702731400153X> (visited on 02/29/2024).
- Hooper, A., P. Segall, and H. Zebker (July 2007). "Persistent Scatterer Interferometric Synthetic Aperture Radar for Crustal Deformation Analysis, with Application to Volcán Alcedo, Galápagos". In: *Journal of Geophysical Research: Solid Earth* 112.B7, 2006JB004763. ISSN: 0148-0227. DOI: [10.1029/2006JB004763](https://doi.org/10.1029/2006JB004763). URL: <https://agupubs.onlinelibrary.wiley.com/doi/10.1029/2006JB004763> (visited on 02/27/2024).
- Hooper, Andrew et al. (Jan. 2012). "Recent Advances in SAR Interferometry Time Series Analysis for Measuring Crustal Deformation". In: *Tectonophysics* 514–517, pp. 1–13. ISSN: 00401951. DOI: [10.1016/j.tecto.2011.10.013](https://doi.org/10.1016/j.tecto.2011.10.013). URL: <https://linkinghub.elsevier.com/retrieve/pii/S0040195111004343> (visited on 02/27/2024).
- Jones, D. R., C. D. Perttunen, and B. E. Stuckman (Oct. 1, 1993). "Lipschitzian Optimization without the Lipschitz Constant". In: *Journal of Optimization Theory and Applications* 79.1, pp. 157–181. ISSN: 1573-2878. DOI: [10.1007/BF00941892](https://doi.org/10.1007/BF00941892). URL: <https://doi.org/10.1007/BF00941892> (visited on 08/29/2024).
- Jones, Donald R. and Joaquim R. R. A. Martins (Mar. 2021). "The DIRECT Algorithm: 25 Years Later". In: *Journal of Global Optimization* 79.3, pp. 521–566. ISSN: 0925-5001, 1573-2916. DOI: [10.1007/s10898-020-00952-6](https://doi.org/10.1007/s10898-020-00952-6). URL: <https://link.springer.com/10.1007/s10898-020-00952-6> (visited on 08/29/2024).
- Kampes, B. and S. Usai (1999). "Doris: The Delft Object-oriented Radar Interferometric Software". In: 2nd International Symposium on Operationalization of Remote Sensing. Enschede, The Netherlands. URL: <http://doris.tudelft.nl/>.
- La Borderie, Christian (2017). "Cast3M, a Multi-Physic Finite Element Program Opened to the Research Community". In: *Heat, Light and Wind Simulation on an Urban Scale*. Anglet, France. URL: <https://univ-pau.hal.science/hal-02153984>.
- McTigue, D. F. (Nov. 10, 1987). "Elastic Stress and Deformation near a Finite Spherical Magma Body: Resolution of the Point Source Paradox". In: *Journal of Geophysical Research: Solid Earth* 92.B12, pp. 12931–12940. ISSN: 0148-0227. DOI: [10.1029/JB092iB12p12931](https://doi.org/10.1029/JB092iB12p12931). URL: <https://agupubs.onlinelibrary.wiley.com/doi/10.1029/JB092iB12p12931> (visited on 02/27/2024).
- Menke, William (2012). *Geophysical Data Analysis: Discrete Inverse Theory*. Matlab ed., 3rd ed. Waltham, MA: Academic Press. ISBN: 978-0-12-397160-9.
- Mogi, Kiyoo (1958). "Relations between the Eruptions of Various Volcanoes and the Deformations of the Ground Surfaces around Them". In: *Earthq Res Inst* 36, pp. 99–134.
- O'Hara, Catherine (2023). "Estimating Deformation Source Parameters Using a 3D Elastic Finite Element Model Including Topography and Crustal Heterogeneity at Askja, Iceland." PhD thesis. URL: <http://hdl.handle.net/1946/45701>.
- Okada, Yoshimitsu (Aug. 1, 1985). "Surface Deformation Due to Shear and Tensile Faults in a Half-Space". In: *Bulletin of the Seismological Society of America* 75.4, pp. 1135–1154. ISSN: 1943-3573, 0037-1106. DOI: [10.1785/BSSA0750041135](https://doi.org/10.1785/BSSA0750041135). URL: <https://pubs.geoscienceworld.org/bssa/article/75/4/1135/118782/Surface-deformation-due-to-shear-and-tensile> (visited on 02/27/2024).
- Parks, Michelle and ISVOLC Team (Mar. 11, 2024). *An Update of Recent Geodetic Observations and Modelling Results at Key Icelandic Volcanoes within the ISVOLC*

- Project. DOI: [10.5194/egusphere-egu24-19525](https://doi.org/10.5194/egusphere-egu24-19525). URL: <https://meetingorganizer.copernicus.org/EGU24/EGU24-19525.html> (visited on 08/30/2024).
- Powell, M. (Jan. 1, 2009). "The BOBYQA Algorithm for Bound Constrained Optimization without Derivatives". In: *Technical Report, Department of Applied Mathematics and Theoretical Physics*.
- Rios, Luis Miguel and Nikolaos V. Sahinidis (July 2013). "Derivative-Free Optimization: A Review of Algorithms and Comparison of Software Implementations". In: *Journal of Global Optimization* 56.3, pp. 1247–1293. ISSN: 0925-5001, 1573-2916. DOI: [10.1007/s10898-012-9951-y](https://doi.org/10.1007/s10898-012-9951-y). URL: <https://link.springer.com/10.1007/s10898-012-9951-y> (visited on 08/29/2024).
- Schmidt, Peter et al. (May 1, 2010). "3D GIA-modelling of Northern Europe with Varying Lithospheric Thickness". In: p. 8802. URL: <https://ui.adsabs.harvard.edu/abs/2010EGUGA..12.8802S> (visited on 08/29/2024).
- Segall, Paul (2010). *Earthquake and Volcano Deformation*. Princeton, N. J: Princeton university press. ISBN: 978-0-691-13302-7.
- (Jan. 7, 2019). "Magma Chambers: What We Can, and Cannot, Learn from Volcano Geodesy". In: *Philosophical Transactions of the Royal Society A: Mathematical, Physical and Engineering Sciences* 377.2139, p. 20180158. DOI: [10.1098/rsta.2018.0158](https://doi.org/10.1098/rsta.2018.0158). URL: <https://royalsocietypublishing.org/doi/full/10.1098/rsta.2018.0158> (visited on 08/30/2024).
- Shahriari, Bobak et al. (Jan. 2016). "Taking the Human Out of the Loop: A Review of Bayesian Optimization". In: *Proceedings of the IEEE* 104.1, pp. 148–175. ISSN: 1558-2256. DOI: [10.1109/JPROC.2015.2494218](https://doi.org/10.1109/JPROC.2015.2494218). URL: <https://ieeexplore.ieee.org/abstract/document/7352306> (visited on 08/30/2024).
- Sigmundsson, Freysteinn (2006). *Iceland Geodynamics: Crustal Deformation and Divergent Plate Tectonics*. Springer-Praxis Books in Geophysical Sciences. Berlin ; New York : Chichester, UK: Springer ; In association with Praxis Pub. 209 pp. ISBN: 978-3-540-24165-2.
- Sigmundsson, Freysteinn, Páll Einarsson, et al. (Feb. 2020). "Geodynamics of Iceland and the Signatures of Plate Spreading". In: *Journal of Volcanology and Geothermal Research* 391, p. 106436. ISSN: 03770273. DOI: [10.1016/j.jvolgeores.2018.08.014](https://doi.org/10.1016/j.jvolgeores.2018.08.014). URL: <https://linkinghub.elsevier.com/retrieve/pii/S0377027317306376> (visited on 02/27/2024).
- Sigmundsson, Freysteinn, Sigrún Hreinsdóttir, et al. (Nov. 2010). "Intrusion Triggering of the 2010 Eyjafjallajökull Explosive Eruption". In: *Nature* 468.7322, pp. 426–430. ISSN: 0028-0836, 1476-4687. DOI: [10.1038/nature09558](https://doi.org/10.1038/nature09558). URL: <https://www.nature.com/articles/nature09558> (visited on 02/27/2024).
- Sigmundsson, Freysteinn, Michelle Parks, Halldór Geirsson, et al. (Feb. 8, 2024). "Fracturing and Tectonic Stress Drives Ultrarapid Magma Flow into Dikes". In: *Science*, eadn2838. ISSN: 0036-8075, 1095-9203. DOI: [10.1126/science.adn2838](https://doi.org/10.1126/science.adn2838). URL: <https://www.science.org/doi/10.1126/science.adn2838> (visited on 02/27/2024).
- Sigmundsson, Freysteinn, Michelle Parks, Rikke Pedersen, et al. (Jan. 1, 2018). "Chapter 11 - Magma Movements in Volcanic Plumbing Systems and Their Associated Ground Deformation and Seismic Patterns". In: *Volcanic and Igneous Plumbing Systems*. Ed. by Steffi Burchardt. Elsevier, pp. 285–322. ISBN: 978-0-12-809749-6. DOI: [10.1016/B978-0-12-809749-6.00011-X](https://doi.org/10.1016/B978-0-12-809749-6.00011-X). URL: <https://www.sciencedirect.com/science/article/pii/B978012809749600011X> (visited on 08/22/2024).

- Sigurðardóttir, Fjóla María (May 2024). “Modelling of Ground Deformation at Eyjafjalljökull Volcano 2011-2015”. BA thesis. Reykjavik: Faculty of Earth Sciences, University of Iceland.
- Valsson, Guðmundur Þór (Mar. 2019). *ISN2016 - Tækniskýrsla*. Íslands: Landmælingar. URL: <https://www.lmi.is/is/um-lmi/frettagfirlit/isn2016-tkniskrsla> (visited on 08/22/2024).
- Van Stein, Bas et al. (2018). “A Novel Uncertainty Quantification Method for Efficient Global Optimization”. In: *Information Processing and Management of Uncertainty in Knowledge-Based Systems. Applications*. Ed. by Jesús Medina et al. Vol. 855. Cham: Springer International Publishing, pp. 480–491. ISBN: 978-3-319-91478-7 978-3-319-91479-4. DOI: [10.1007/978-3-319-91479-4_40](https://doi.org/10.1007/978-3-319-91479-4_40). URL: https://link.springer.com/10.1007/978-3-319-91479-4_40 (visited on 08/30/2024).
- Xiang, Y. and X. G. Gong (Sept. 1, 2000). “Efficiency of Generalized Simulated Annealing”. In: *Physical Review E* 62.3, pp. 4473–4476. DOI: [10.1103/PhysRevE.62.4473](https://doi.org/10.1103/PhysRevE.62.4473). URL: <https://link.aps.org/doi/10.1103/PhysRevE.62.4473> (visited on 08/30/2024).